Computational Study of the Vertical Axis Wind Turbines: Wake Dynamics and Generated Torque

Pooya Ahmadi

A Thesis

in

The Department

of

Mechanical and Industrial Engineering

Presented in Partial Fulfillment of the Requirements

for the Degree of Master of Applied Science (Mechanical Engineering) at

Concordia University

Montreal, Quebec, Canada

March 2013

CONCORDIA UNIVERSITY

School of Graduate Studies

This is to certify that the thesis prepared

By: Pooya Ahmadi

Entitled: Computational Study of the Vertical Axis Wind Turbines: Wake Dynamics and Generated Torque

and submitted in partial fulfillment of the requirements for the degree of

Master of Applied Science (Mechanical Engineering)

complies with the regulations of the University and meets the accepted standards with respect to originality and quality.

Signed by the final Examining Committee:

_____ Chair

Dr. Hoi Dick Ng

_____ Examiner

Dr. S. Samuel Li

_____ Examiner

Dr. Ali Dolatabadi

_____ Supervisor

Prof. Marius Paraschivoiu

Approved by _____

Chair of Department or Graduate Program Director

_____ 2013 _____

Dean of Faculty

ABSTRACT

Computational Study of the Vertical Axis Wind Turbines: Wake Dynamics and Generated Torque

Pooya Ahmadi

A computational study of the aerodynamics of the straight-bladed VAWTs was performed by RNG $k-\varepsilon$ and S-A turbulence models. Three different rotor types with NACA0022, NACA0018, and S1223 blade profiles were studied. The main objective was to numerically analyse the torque and the highly unsteady wake-dynamics of the VAWTs by RANS turbulence models. The effect of increasing the blockage of the free-stream wind by the rotor on the generated torque, the influence of different turbulence models on the results, and the performance of the downwind rotor in a row of two VAWTs were analysed as well.

The results indicate that the ducted VAWTs are more efficient than the regular VAWTs. The efficiency of the rotor is overestimated by the 2-D geometry. This is mainly related to the negative influence of the tip vortices on the torque. The velocity magnitude in the wake recovers 50 % of its inlet value within $2D$ downstream distance. In a row of 2 VAWTs, due to the disturbances in the flow generated by a turbine placed $15D$ upwind, the efficiency of the downstream VAWT varies in each revolution of the rotor. Comparison between the values of torque obtained by the RNG $k-\varepsilon$ and S-A turbulence models reveals that the RNG $k-\varepsilon$ model reports higher values of torque. In a direct relation, the values of torque obtained by the second-order-accurate solver are generally higher than those given by the first-order solvers. It can be argued that although the RANS turbulence models overestimate the efficiency, they can be appropriately used as CFD design tools.

To my parents

for their endless support and encouragement

Acknowledgements

I would like to express my sincere gratitude to Professor Marius Paraschivoiu for his invaluable advice, constant support, and encouragement throughout my studies at Concordia University.

Contents

List of Figures

List of Tables

Nomenclature

$\vec{\omega}$ vorticity

G_ν production of turbulent viscosity

$S_{\tilde{\nu}}$ user-defined source term

Y_ν destruction of turbulent viscosity

α angle of attack

α_k inverse effective Prandtl number for k

α_ε inverse effective Prandtl numbers for ε

δ_{ij} Kronecker delta

λ tip speed ratio

μ dynamic viscosity of the working fluid

μ_{eff} effective viscosity

μ_t turbulence viscosity

ν molecular kinematic viscosity

ω angular velocity of the rotor

Ω_{ij} mean rate-of-rotation tensor

ρ density of the working fluid

σ solidity of the VAWTs

$\sigma_{\tilde{\nu}}$,κ,C_{b1},C_{b2},C_{prod},$C_{\nu 1}$,C_{w1}, C_{w2},C_{w3} model constants for S-A model

θ azimuth angle

θ_{Crit} the azimuthal location where torque from a single blade reaches its maximum

$\tilde{\nu}$ modified turbulence kinematic viscosity

ε turbulence dissipation rate

C chord length

C_p power coefficient

C_Q torque coefficient

$C_{1\varepsilon}$, $C_{2\varepsilon}$, η_0, β the model constants for the RNG $k-\varepsilon$ model

D rotor diameter

d distance from the wall

D_h hydraulic diameter

dt time step size

dx chord-wise mesh step size around the blade

$f_{\nu 1}$ viscous damping function

G_b the generation of turbulence kinetic energy due to buoyancy

G_k generation of turbulence kinetic energy due to the mean velocity gradients

I turbulence intensity

k kinetic energy of turbulence

L lateral (cross-wind) position zeroed at the rotor center

Ma Mach number

N number of blades

R rotor radius

Re Reynolds number

S scalar measure of the deformation

S_k and S_ε user-defined source terms in the formulation of the RNG $k-\varepsilon$ model

S_{ij} mean strain rate

T_b torque generated by a single blade

T_t total torque generated by the turbine

U velocity magnitude of air

$u_i^{'}$,$u_j^{'}$ components of velocity fluctuations

u_i,u_j components of velocity

U_x cross-stream component of velocity

U_y stream-wise component of velocity

U_∞ free-stream velocity magnitude

V_{rel} relative velocity of the wind with respect to the rotating blade

x distance measured from the leading edge of the airfoil along the chord length

y^+ non-dimensionalized distance from the wall

Y_M dilatation dissipation

1 Introduction

1.1 Wind Turbines

The two major types of wind turbines are horizontal-axis wind turbines (HAWTs) and vertical-axis wind turbines (VAWTs). HAWTs are turbines with the blades rotating around an axis parallel to the ground i.e. a horizontal axis. The blades of a VAWT rotate around an axis perpendicular to the ground i.e. a vertical axis [3]. Another interpretation of the difference between these two types of wind turbines can be related to the orthogonality of the free-stream velocity to the rotor plane. For HAWTs, the wind velocity vector is perpendicular to the rotor plane. Nevertheless, for VAWTs, the free-stream velocity moves parallel to the rotor plane. Several types of VAWTs are available. This work aims at analysis of the major available and used type of VAWTs i.e. straight-bladed VAWTs.

1.2 Motivation

To date, high demands for power have created new motivations to find alternative approaches for power generation and to optimize the existing methods. Ducted VAWTs can be used to generate electricity from the air flow in the buoyancy-driven ventilation systems. Accordingly, analysis of aerodynamics and performance of ducted VAWT is of interest. Alternatively, VAWT can be good candidates for generation of electricity due to their particular advantages over HAWTs. Specifically, VAWTs can be placed closer to each other due to the fact that they can function adequately in non-uniform wind fields. Moreover, VAWTs are not restricted by the direction of the wind. Nevertheless, they inherit highly complex aerodynamics related to the dynamic stall at different azimuthal locations. Then, VAWTs produce less noise than their horizontal counterparts [4].

Power output from wind farms operated by HAWTs is highly dependent upon the downstream spacing of the wind turbines [5]. Reducing the downstream spacing of a row of HAWTs from 10D to 5D may decrease the power output by approximately 40% [5] . VAWTs are preferred because of their lower height that can be up to 10 times lower that the height of typical HAWTs within comparable ranges of efficiency.

Current renewable energy resources, specially the wind farms using HAWTs, require wide areas of land in order to extract considerable amount of energy [3]. This is due to the fact that in order to achieve 90% of the torque output of a single isolated HAWT of rotor diameter D in a HAWT wind farm, a turbine must be located at $3D$ to $5D$ in cross-wind direction and $6D$ to $10D$ in the downwind direction away from the other wind turbines [3]. Therefore, wind farms have to be located at remote locations away from the high-energy-demanding areas [3].

VAWTs can offer higher power densities than their horizontal counterparts [3]. More precisely, VAWTs can be placed close to each other in a wind farm operated by VAWTs and so the overall power output of the wind farm per unit land area can be considerably increased. Also, VAWTs are not restricted by the direction of the wind and they can operate by wind from any direction [6]. Therefore, they do not need to have a complicated yawing system [6]. In comparison to HAWTs, VAWTs possess a simpler structure that makes their production and maintenance easier [6]. Another major advantage of VAWTs over HAWTs is that the turbine's generator does not have to be on top of the tower. The generator can be mounted on the ground that can simplify the structure of the tower and reduce its manufacturing costs. Nevertheless, VAWTs incorporate highly complex, unsteady, and non-linear aerodynamic behaviour [6]. Thus, numerical analysis of aerodynamics of the VAWTs can provide a deeper insight into this phenomenon.

Alternatively, specification of the minimum downwind spacing required for the maximum possible power output from the downstream turbines can lead to generation of more energy from smaller pieces of land. This achievement can be quite beneficial for small and high-energy-demanding areas.

1.3 Aims and Objectives

This study is dedicated to computational analysis of the aerodynamics of VAWTs using 2-D and 3-D geometries. This work is not aimed at comparative analysis of performance of the VAWTs. The main objective is to numerically analyse the highly unsteady aerodynamics of the VAWTs by Boussinesq hypothesis-based turbulence modelling. Two major areas of interest i.e. the torque generated by the VAWTs and the flow disturbances in the wake are to be specifically investigated. In this regard, velocity field, the intensity of the turbulence, and vorticity in the wake are the major quantities of interest. Numerical estimation and analysis of the torque generated by each blade and the effect of the wake of an upwind rotor on the efficiency of the downwind VAWT are the other targets of this study.

1.4 History

The entire information about the history of the wind turbines presented in this section are from Manwell et al. [7]. Windmills were invented by the Persians in approximately 900 AD. The first windmills were drag-type mills with vertical axes. Wind energy was recognized in Europe during the middle ages. These mills that had horizontal axes were used for mechanical tasks e.g. grain grinding. A typical European windmill had 4 blades [7].

Although the European windmills had developed high-level designs, they were no longer much appreciated in Europe after the Industrial Revolution. The reason

behind this was that wind energy could not be transported. Coal, a portable fossil fuel, was the alternative to the non-dispatchable wind energy [7].

The invention of electrical generators about the end of the nineteenth century was the first step for using the wind energy for generation of electricity. United Stated, Denmark and Germany had noticeable contributions to development of early electricity-generating wind turbines [7].

In the late 1960s, people became aware of the consequences of the industrial development. At this time, polluting fossil fuels and potentially dangerous nuclear energy were recognised as not-so-appropriate sources of energy by many people. These concerns led to a wider search for cleaner sources of energy [7].

At the end of the 20th century, wind turbine technology took advantage of developments in other areas of science. Materials science helped build new composites and alloys for the blades and metal components, respectively. Advances in computer science made design, analysis, and control of the wind turbines easier. Aerospace industry with aerodynamic design methods started to participate in wind turbine technology. Analytical methods began to provide a more vivid understanding of the performance of the new designs. Sensors and data analysis equipment helped designers in understanding the performance of the newly-developed wind turbines. Power electronic devices could help with the connection of the wind turbines' generators to the electrical network. Thus, wind turbines were brought to a whole new generation [7].

Although wind turbine technology has developed to a high level over the past 35 years, it still can be evolved. There still is space for reducing the cost of energy. Wind turbines can perform at lower wind speeds. Turbines can be more cost effective for all applications. Engineering methods can be improved for design, analysis, and mass production of the turbines. Material science may be able to

increase the lifetime of the turbine [7].

1.5 Thesis Outline

In this work, the Introduction section is followed by the Aerodynamic background. Then, the methods of the simulation and evaluation of the results are discussed in Methods section. After that, in the Verification and Validation section, the results are verified and compared with the related published numerical and experimental data available in the literature. This section is followed by the Results. The section begins with analysis of a ducted VAWT, after which the effect of different turbulence models on the generated blade torque is discussed. Aerodynamics of the wake is discussed in this section as well. Then, results obtained from 2-D and 3-D geometries are compared and the efficiency of downwind rotor in a row of two VAWTs is discussed. After that, the conclusions are followed by the suggested future work.

2 Aerodynamic Background

2.1 Dynamic-Stall

The aerodynamics of VAWTs are highly unsteady. This is due to the fact that the angle of attack, α, varies with the azimuth angle, θ, and affects the relative velocity, V_{rel}, and consequently the Reynolds number [8]. The dynamic-stall is caused by the separation of the boundary layer that occurs during the unsteady motion of the blades [9]. The dynamic-stall is associated with the shedding and passage of flow disturbances along the suction surface of the airfoil [9]. The shedding of these vortex-like disturbances is the apparent characteristic of the dynamic-stall [9]. This phenomenon is dependant upon the parameters related to the rotation of the blades and those concerning the boundary-layer separation [9]. The former includes the motion type, maximum angle, and reduced frequency [9]. The latter implies the type of the airfoil and Re and Ma numbers [9] . The specific features of the dynamic-stall obtained by a typical study of a Vertol $VR-7$ airfoil discussed in the following paragraph are from Paraschivoiu [9].

In the upstroke motion of the blade, the flow reverses inside the boundary layer. Nevertheless, it remains attached beyond the point it separates in steady flow. As the blade rotates further, a vortex appears around the leading edge of the airfoil and it passes over the blade with a velocity of approximately 0.22 of free-stream velocity. Then, this vortex separates from the airfoil and sheds into the wake. After that, a vortex rotating in an opposite direction develops at the trailing edge and interacts. During the downstroke motion of the airfoil, weaker and higher order vortices originate at either the leading edge or trailing edge of the airfoil creating clockwise and counter clockwise vortices, respectively [9]. The flow from the leading edge to the trailing edge remains mainly separated during

the downstroke. The flow reattaches to the airfoil in the final azimuthal locations in the cycle [9].

The variation of angle of attack, α with the azimuth angle, θ for a rotating blade at tip speed ratio, λ can be obtained from:

$$\alpha = tan^{-1}\frac{sin(\theta)}{\lambda + cos(\theta)} \tag{1}$$

Figure 1 illustrates the angle of attack versus azimuth angle for different values of λ. The zero position of the azimuth angle, θ, with respect to the direction of the wind is illustrated in figure 2. The dynamic stall is less prone to happen at high values of λ. Nevertheless, the physical constraints such as structural failure due to the centrifugal acceleration put a limit on the maximum angular velocity of the rotor.

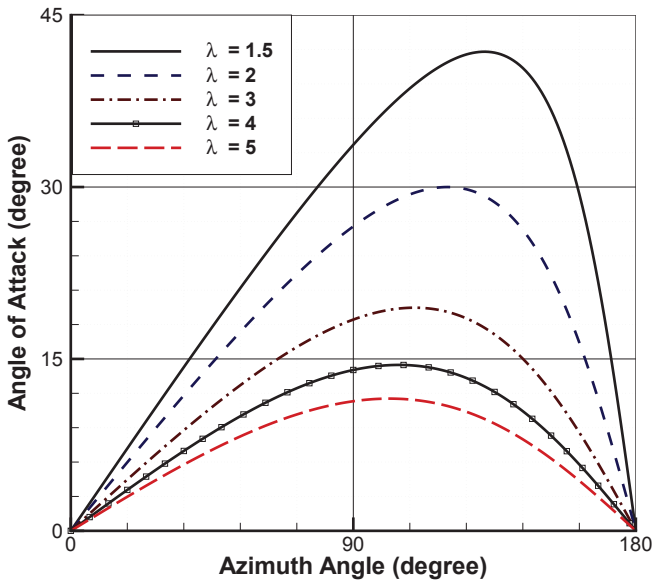

Figure 1: Angle of attack versus azimuth angle for different values of λ

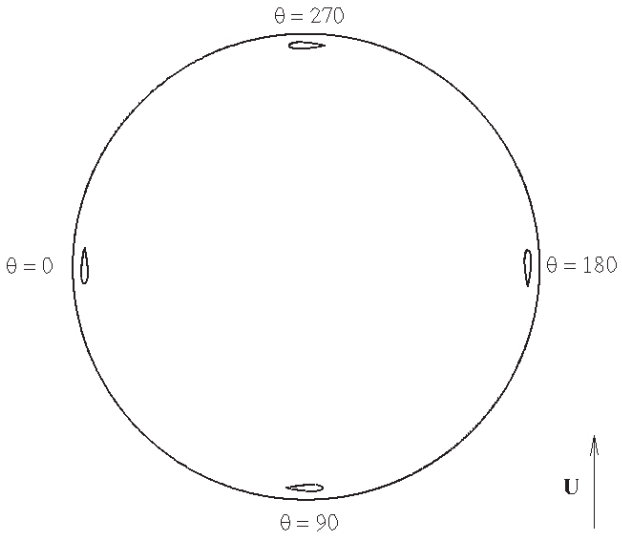

Figure 2: the schematic top view of the rotor (not to scale)

2.2 Torque Generated by the VAWTs

The torque output from the rotor is generated by the pressure and viscous forces. The pressure forces acting on the blades are considerably higher than the viscous forces. Studies reveal that the torque output from straight-bladed VAWT exhibits fluctuations as well as periodicity.

Ji and Schluter [1] investigated a 4-bladed H-rotor of radius 0.2 m and of blade chord length of 0.1 m with S1223 blade profile. Their 2-D results suggest that the torque output is fluctuating and periodical with its maximum generated by a single blade at about 72° azimuthal location.

Howell et. al. [10], performed a numerical and experimental analysis of a small VAWT by NACA 0022 airfoil. The corresponding results indicate that the 2-D simulations predict higher values of performance coefficient with respect to 3-D numerical and experimental analysis [10]. The main reason has been identified as the absence of efficiency-reducing tip vortices in 2-D analysis [10]. The experimental

results in the corresponding work suggest that the surface roughness can enhance the efficiency of the rotor for the Reynolds number range of $Re < 30,000$ [10]. Inversely, the surface roughness results in a reduced efficiency for $Re > 30,000$ [10].

2.3 Tip Vortices

Mertens et.al. [11] showed that in a specific range of the skew angle, a VAWT can produce higher power in skewed flows than in non-skewed flows. Similar to the work of Mertens et.al. [11], the operation of VAWTs in skewed flow was studied by Ferreira et. al. [12]. This study was aimed for application of the VAWTs in the built environment. Authors have claimed that the analysis of the complex aerodynamics of the wind turbines in the built environment is immature. The VAWTs can be preferred for use in built environment [12]. This is mainly due to the fact that the VAWTs are insensitive to flow direction and they do not require a complex yawing system [12].

Unlike the majority of the researches on the VAWTs that assume a perpendicular flow to the rotor's axis, Ferreira et. al. [12] worked on analysis of the aerodynamics of the turbine in skewed flow. The turbine model was a two-bladed H-rotor with a diameter of $0.75m$ and a height of $0.5m$. The blade profile was NACA 0018 with zero pitch. The tip speed ratios were 3.07, 3.11, and 3.27 for non-skewed flow case, 15° skewed flow case, and 30° skewed flow case, respectively. In the corresponding work, the study was accomplished by smoke visualization of the tip vortex expansion, hotwire measurements of the flow, and thrust force measurement of the VAWTs [12]. The experiments were performed in a wind tunnel of $2.24m$ diameter. The wind velocity was 7 m/s with the turbulence level being in between 1.2 % and 1.7 %.

The experimental results of Ferreira [12] illustrate the tip vortices generated

by the interaction of the flow with the blade at its most upwind location at 8 different azimuthal locations i.e. 40°, 34°, 30°, 13°, 35°, 51°, 56°, and 90°. The the tip vortex expands as it moves in the downwind direction and it does not significantly dissipate after interaction with the downwind passing blade [12]. The vortex core moves in the direction of the free-stream flow [12].

2.4 The Level of Turbulence

The level of turbulence of the flow can be determined by the non-dimensional Reynolds number, Re. It can be calculated based on the chord length of the airfoil according to:

$$Re = \frac{\rho V_{rel} x}{\mu}$$

where ρ is the density of the fluid, V_{rel} is the relative velocity of the wind with respect to the rotating blade, x is the distance measured along the chord length from the leading edge of the airfoil towards the trailing edge, and μ is the dynamic viscosity of the fluid.

The upper and lower limits of the Re number during each revolution of the rotor can be determined using the minimum and maximum values of V_{rel}. The minimum and maximum values of V_{rel} occur at $\theta = 180°$ and $\theta = 0°$, respectively, therefore:

$$R\omega - U_\infty < V_{rel} < R\omega + U_\infty$$

where U_∞ is the free-stream wind velocity, accordingly:

$$\frac{\rho(R\omega - U_\infty)x}{\mu} < Re < \frac{\rho(R\omega + U_\infty)x}{\mu}$$

2.5 Computational Fluid Dynamics for the VAWTs

There are many methods to observe the irregularity, unsteadiness and unpredictability of turbulent flows. Amongst the numerical methods, Reynolds-averaged Navier-Srokes (RANS) turbulence models as well as large eddy simulation (LES) are of particular popularity for computational analysis of aerodynamics of VAWT. The former provides satisfactory agreement with experimental results for a wide range of flow problems in expense of reasonable computational power. The latter, although with the current computational power is considered expensive, is widely used to capture the tip vortices and flow disturbances in the wake.

The Spalart-Allmaras (S-A) model discussed in Spalart and Allmaras [13] is proved to perform well in the near-wall regions of the flow and is one of the most reliable turbulence models for simulation of the flows around the blades. Among the RANS models, the Renormalization group (RNG) $k-\varepsilon$ model is widely used for analysis of the aerodynamics of VAWT. The renormalization group (RNG) $k-\varepsilon$ model discussed in Yakhot, V. and Orszag, S.A. [14] and Orszag, S.A et al. [15] is one of the variants of the standard $k-\varepsilon$ model by Launder and Spalding [16]. In the RNG $k-\varepsilon$ model, formulation of the transport equation for turbulence dissipation rate, ε, was improved to better handle the flows that are subject to rapid strains and streamline curvature [17]. This modification makes the RNG $k-\varepsilon$ model a good candidate for the analysis of the wind turbine wakes within affordable computational power. The formulations for the two transport equations for the turbulence kinetic energy, k, and turbulence dissipation rate, ε of the RNG $k-\varepsilon$ model is analysed further in the text. Since the VAWT function at very low Mach numbers, the flow can be considered as incompressible in the above-mentioned models.

The present study was performed by the RNG $k-\varepsilon$ and S-A turbulence models.

The unavoidable computational expense of the LES model was the main reason it was not employed for the analysis of the wake in this work.

3 Methods

3.1 The Turbulence Models

3.1.1 Spalart-Allmaras Model

The Spalart-Allmaras (S-A) model proposed by Spalart and Allmaras [13] takes advantage of a modelled transport equation for turbulent viscosity, μ_t [17]. All the formulations in this section are from [13] and [17], to which the reader is referred to for more details. The S-A model is derived using the Boussinesq hypothesis that relates the Reynolds stresses to the mean velocity gradients as:

$$-\rho\overline{u_i' u_j'} = \mu_t \left(\frac{\partial u_i}{\partial x_j} + \frac{\partial u_j}{\partial x_i} \right) - \frac{2}{3} \left(\rho k + \mu_t \frac{\partial u_k}{\partial x_k} \right) \delta_{ij} \tag{2}$$

Application of Boussinesq hypothesis leads to lower computational cost for computation of the turbulent viscosity, μ_t [17]. In this method, μ_t is assumed as an isotropic scalar quantity that is considered to be effective for shear flows that are highly affected by only one of the turbulent shear stresses [17]. Wall boundary layer flows are good examples of this type of flow [17]. Nevertheless, when the flow is considerably influenced by the anisotropy of turbulence, e.g. in highly swirling flows, the Boussinesq hypothesis may provide less accurate results [17].

In Spalart-Allmaras model, the transport equation for the modified turbulent kinematic viscosity, $\tilde{\nu}$, is:

$$\begin{aligned} &\frac{\partial}{\partial t}(\rho\tilde{\nu}) + \frac{\partial}{\partial x_i}(\rho\tilde{\nu}u_i) = \\ &\qquad G_\nu - Y_\nu + S_{\tilde{\nu}} + \frac{1}{\sigma_{\tilde{\nu}}} \left[\frac{\partial}{\partial x_j} \left((\mu + \rho\tilde{\nu}) \frac{\partial \tilde{\nu}}{\partial x_j} \right) + C_{b2}\rho \left(\frac{\partial \tilde{\nu}}{\partial x_j} \right)^2 \right] \end{aligned} \tag{3}$$

in which G_ν and Y_ν are the production and destruction of turbulent viscosity in

the near-wall region of the flow, respectively. G_ν can be obtained from:

$$G_\nu = C_{b1}\rho\tilde{S}\tilde{\nu} \tag{4}$$

where

$$\tilde{S} = S + \frac{\tilde{\nu}}{\kappa^2 d^2} f_{\nu 2}$$

and

$$f_{\nu 2} = 1 - \frac{\chi}{1 + \chi f_{\nu 1}}$$

$\sigma_{\tilde{\nu}} = 0.666$, $\kappa = 0.4187$, $C_{b1} = 0.1355$, and $C_{b2} = 0.622$ are the model constants and d is the distance from the wall. $S_{\tilde{\nu}}$ is a user-defined source term and S is a scalar measure of the deformation given by:

$$S = \sqrt{2\Omega_{ij}\Omega_{ij}} \tag{5}$$

where Ω_{ij} is the mean rate-of-rotation tensor and is computed from:

$$\Omega_{ij} = \frac{1}{2}\left(\frac{\partial u_i}{\partial x_j} - \frac{\partial u_j}{\partial x_i}\right)$$

The formulation of the scalar measure of the deformation tensor given by equation (5) indicates that vorticity and the rate of strain are identical in shear flows [17]. In inviscid regions of the flow, e.g. stagnation lines, vorticity is zero and the strain rate can result in non-physical production of turbulence [17]. Thus, the formulation of S is modified to incorporate the measures of strain tensors and vorticity:

$$S = |\Omega_{ij}| + C_{prod} min\left(0, |S_{ij}| - |\Omega_{ij}|\right) \tag{6}$$

where $C_{prod} = 2.0$,

$$|\Omega_{ij}| = \sqrt{2\Omega_{ij}\Omega_{ij}}$$

and

$$|S_{ij}| = \sqrt{2S_{ij}S_{ij}}$$

in which

$$S_{ij} = \frac{1}{2}\left(\frac{\partial u_j}{\partial x_i} - \frac{\partial u_i}{\partial x_j}\right)$$

is the mean strain rate. Then, the turbulent viscosity is obtained from

$$\mu_t = \rho\tilde{\nu} f_{\nu 1} \tag{7}$$

where $f_{\nu 1}$ is the viscous damping function computed from:

$$f_{\nu 1} = \frac{\chi^3}{\chi^3 + C_{\nu 1}^3}$$

in which

$$\chi = \frac{\tilde{\nu}}{\nu}$$

In the above formulations, ν is the molecular kinematic viscosity and $C_{\nu 1} = 7.1$ is the model constant.

The destruction of turbulent viscosity is given by:

$$Y_\nu = C_{w1}\rho f_w (\frac{\tilde{\nu}}{d})^2 \tag{8}$$

in which

$$f_w = g\left(\frac{1 + C_{w3}^6}{g^6 + C_{w3}^6}\right)^{1/6}$$

, where

$$g = r + C_{w2}\left(r^6 - r\right)$$

and

$$r = \frac{\tilde{\nu}}{\tilde{S}\kappa^2 d^2}$$

In these relations, $C_{w1} = 3.2059$, $C_{w2} = 0.3$, and $C_{w3} = 2.0$ are model constants.

3.1.2 RNG $k - \varepsilon$ Model

The renormalization group (RNG)$k - \varepsilon$ model discussed in Yakhot, V. and Orszag, S.A. [14] and Orszag, S.A et al. [15] is one of the variants of the standard $k-\varepsilon$ model proposed by Launder and Spalding [16]. All the formulations presented in this section are from [17], [15], and [14].

The RNG $k-\varepsilon$ model incorporates two transport equations for the turbulence kinetic energy, k, and turbulence dissipation rate, ε. The RNG $k - \varepsilon$ model was modified to better handle the rapidly strained and swirling flows [17]. In the RNG $k-\varepsilon$ model, formulation of the transport equation for turbulence dissipation rate, ε, was improved to better handle the flows that are subject to rapid strains and streamline curvature [17]. This modification that is incorporated in the last term of equation (10), makes the RNG $k - \varepsilon$ model a good candidate for the analysis of the wind turbine wakes within affordable computational power. Also, this model takes advantage of an analytically-derived turbulent Prandtl number and an analytical differential formula for effective viscosity that takes care of the low-Reynolds-number effects [17].

The transport equations for the RNG $k - \varepsilon$ model are

$$\frac{\partial}{\partial t}(\rho k) + \frac{\partial}{\partial x_i}(\rho k u_i) = \frac{\partial}{\partial x_j}\left(\alpha_k \mu_{eff} \frac{\partial k}{\partial x_j}\right) + G_k + G_b - \rho\varepsilon - Y_M + S_k \quad (9)$$

and

$$\frac{\partial}{\partial t}(\rho\varepsilon) + \frac{\partial}{\partial x_i}(\rho\varepsilon u_i) =$$
$$\frac{\partial}{\partial x_j}\left(\alpha_\varepsilon \mu_{eff} \frac{\partial \varepsilon}{\partial x_j}\right) + C_{1\varepsilon}\frac{\varepsilon}{k}\left(G_k + C_{3\varepsilon} G_b\right) - \rho\frac{\varepsilon^2}{k}\left(C_{2\varepsilon} + \frac{C_\mu \eta^3 \left(1 - \eta/\eta_0\right)}{1 + \beta\eta^3}\right) \quad (10)$$

In these formulations, the model constants are $C_{1\varepsilon} = 1.42$, $C_{2\varepsilon} = 1.68$, $\eta_0 = 4.38$, and $\beta = 0.012$. The generation of turbulence kinetic energy due to the mean velocity gradients, G_k, can be obtained from the exact equation for the transport of k as:

$$G_k = -\rho\overline{u_i' u_j'}\left(\frac{\partial u_j}{\partial x_i}\right)$$

In order to make G_k consistent with the Boussinesq hypothesis, it is formulated as

$$G_k = \mu_t S^2$$

in which

$$S = \sqrt{2 S_{ij} S_{ij}}$$

is the modulus of the mean rate-of-strain tensor. G_b is the generation of turbulence kinetic energy due to buoyancy. G_b is present in equation (9) when the flow experiences a gravity field and a temperature gradient at the same time [17]. In this simulation, the effect of gravity is neglected. Thus, G_b has a null value.

The dilatation dissipation, Y_M, is responsible for the effects of compressibility on turbulence in high-Mach-number flows [17]. This simulation incorporates the

incompressible-flow assumption that leads to a null value for Y_M in the transport equation for k. In these formulations, S_k and S_ε are user-defined source terms. The terms α_k and α_ε are inverse effective Prandtl numbers for k and ε, respectively and are given by an analytical formula from the RNG theory as:

$$|\frac{\alpha - 1.3929}{\alpha_0 - 1.3929}|^{0.6321}|\frac{\alpha + 2.3929}{\alpha_0 + 2.3929}|^{0.3679} = \frac{\mu_{mol}}{\mu_{eff}} \tag{11}$$

in which $\alpha_0 = 1.0$.

The turbulent viscosity, μ_t, is calculated from:

$$\mu_t = \rho C_\mu \frac{k^2}{\varepsilon} \tag{12}$$

in which $C_\mu = 0.0845$ is the analytically-derived model constant. In equation (10), the term η is defined as:

$$\eta = S\frac{k}{\varepsilon}$$

In comparison to the standard $k-\varepsilon$ model, in highly strained flows i.e. in regions where $\eta > \eta_0$, the modifications in the formulation of RNG $k-\varepsilon$ model that are incorporated in the last term of equation (10) lead to smaller destruction of ε and so to augmentation of ε [17]. This effect leads to decrease in k, and eventually destruction of μ_t [17]. Thus, the RNG $k-\varepsilon$ model is a good candidate for computational analysis of the flows that are affected by streamline curvature and rapid strain [17]. Nonetheless, in weakly to moderately regions of the flow that correspond to regions where $\eta < \eta_0$, the results from the standard $k-\varepsilon$ and RNG $k-\varepsilon$ models are comparable [17].

3.2 Non-Dimensional Parameters

3.2.1 Power Coefficient

The efficiency of the turbine was studied by the power coefficient, C_p. C_p is defined as a function of the rotor swept area, A, air density, ρ, free stream velocity, U_∞, total torque obtained from the turbine, T_t, and the angular velocity of the blades, ω, and is given by:

$$C_p = \frac{\omega T_t}{\frac{1}{2}\rho A V^3} \tag{13}$$

3.2.2 Torque Coefficient

The Torque Coefficient, C_Q was calculated according to:

$$C_Q = \frac{T_b}{\frac{1}{2}\rho R A V^2} \tag{14}$$

where T_b is the blade torque.

3.2.3 Tip Speed Ratio

The tip steep ratio, λ, abbreviated as TSR is a non-dimensional parameter that relates the tangential velocity of the rotor blades to the free-steam velocity, U_∞. It is defined as:

$$\lambda = \frac{R\omega}{U_\infty} \tag{15}$$

where R is the radius of the rotor.

3.2.4 Solidity

Solidity of a straight-blades VAWT can be calculated according to:

$$\sigma = \frac{NC}{R} \tag{16}$$

where N is the number of blades and C is the chord length of the rotor blade.

3.3 The Geometry

Simulations were undertaken for 2-D and 3-D geometries. Three different rotor geometries, namely M23, M18, and M22 models were investigated. The geometries were generated and meshed in Gambit®. The mesh size and its effect on the results is discussed further in the text in sections 4 and 5. The M23 model was selected to verify the computational approach for the simulation by comparing the results with the data available in the literature. The M22 model was chosen to validate the results with experimental data. The M18 model was used for analysis of the ducted versus non-ducted VAWTs with 2-D and 3-D geometries.

3.3.1 M23 Model

The M23 model is an H-Rotor of radius $R = 0.2$ m with S1223 blade profile. The rotor geometry of M23 model is from Ji and Schluter [1]. The chord size is 0.1 m providing a solidity of $\sigma = 2$. The computational domain is extended from five rotor diameters upwind to 10 rotor diameters downwind of the turbine. Figure (3) shows the top view of the rotor with the blades numbered for future reference in the text. The zero position of azimuth angle corresponds to the position of blade 1.

The model was discretized with four different mesh sizes. The very coarse mesh has approximately 280,000 computational cells. The coarse and fine meshes have approximately 1.2 millions and 2 millions mesh cells, respectively. The very fine mesh in this study has 4 million cells.

Figure 8 illustrates the mesh around the S1223 airfoil. The geometry was divided into two zones, i.e. a stationary zone and a rotating plane. The rotor

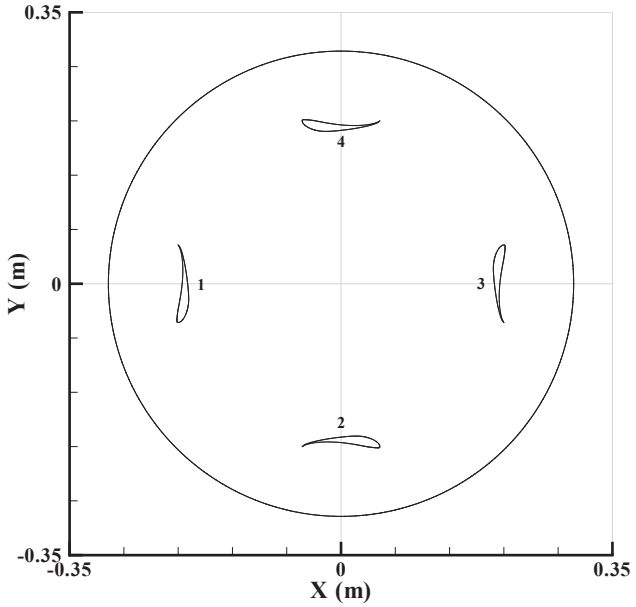

Figure 3: Top view of the rotor with S1223 blade profile

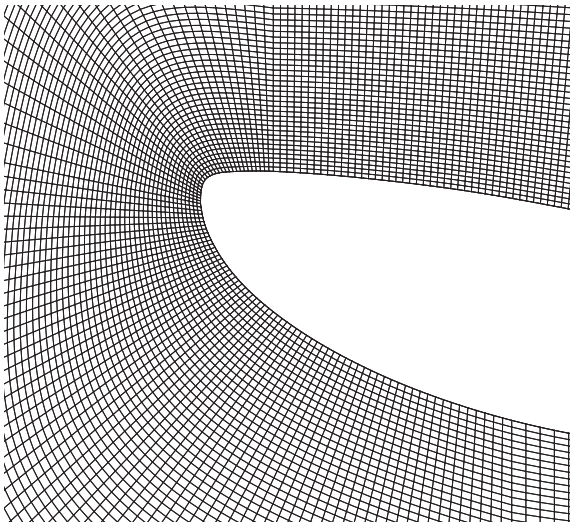

Figure 4: Mesh scheme around the leading edge of S1223 blade profile

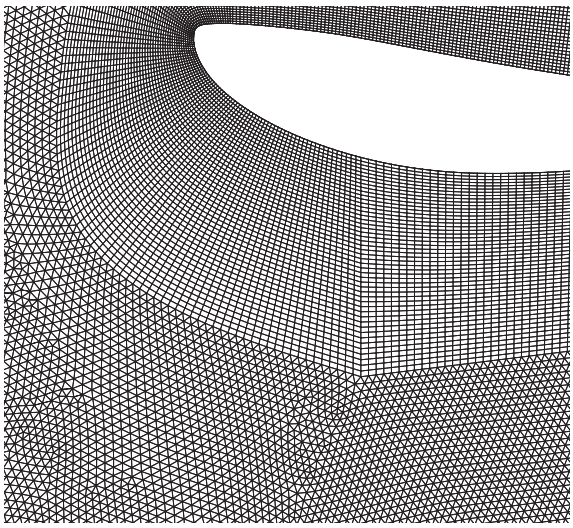

Figure 5: Mesh scheme around S1223 blade profile

was inserted in a rotating plane forming a sliding interface with the rest of the computational domain that was set to be stationary.

As demonstrated in Figure (4), the mesh was structured around the blades. Triangular scheme was used to mesh the rotor area (Figure (5)), beyond which uniform structured mesh was used to capture the wake.

The blades were considered as walls with no-slip condition. In order to capture the viscous sublayer in the near-wall regions of the flow, the value of the non-dimensionalized distance from the wall, $y+$, was kept lower than 1.5 for all blades.

3.3.2 M18 Model

The M18 model is a 4-bladed VAWT, namely a 4-bladed H-Rotor of radius $R = 1$ m in a rectangular duct. Figure (6) shows the top view of the rotor with the blades numbered for future reference in the text. The dashed line connecting the rotor center to blade 1 represents the zero position of the azimuth angle, θ.

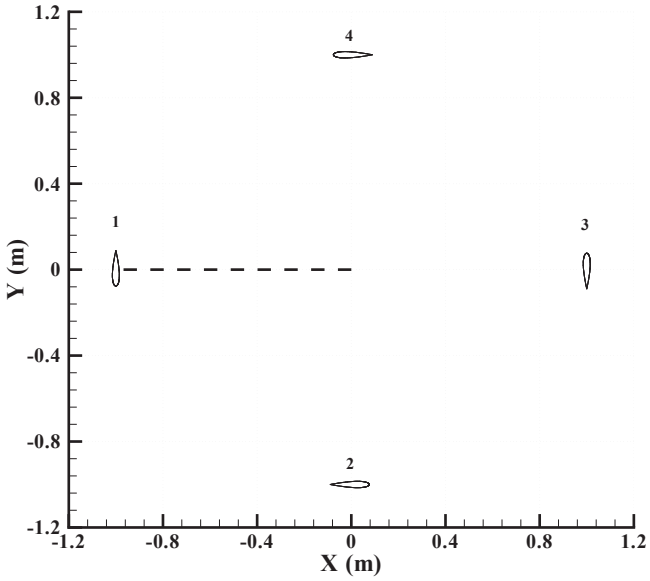

Figure 6: Top view of the rotor with NACA 0018 blade profile (zero position of the azimuthal location is indicated by the dashed line and the flow is in positive y direction)

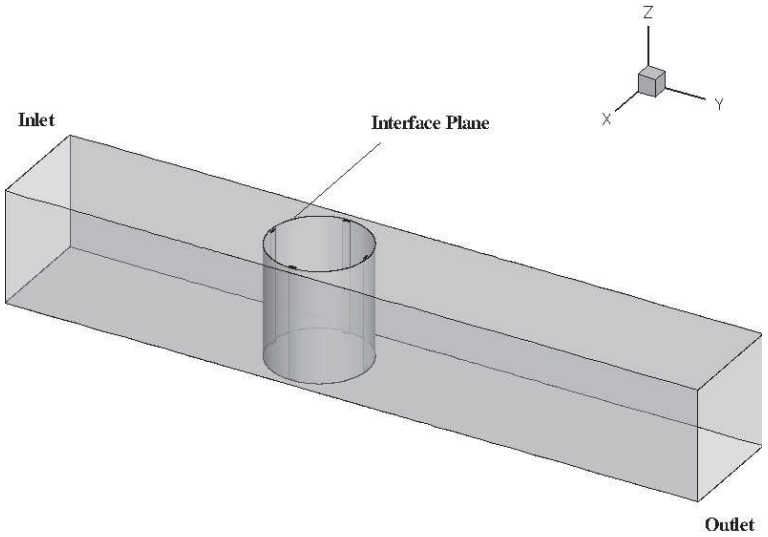

Figure 7: The 3-D geometry with NACA 0018 blade profile

This model was investigated with 2-D and 3-D geometries. The solidity of the rotor is $\sigma = 0.64$. The 3-D geometry of this model that is a straight extrusion of the 2-D model is illustrated in Figure (7). The blades are straight extrusions of NACA 0018 with a uniform chord size of 0.16 m and a span size of equal to duct edge length, forming zero clearance space with the walls. This configuration was selected in order to increase the blade span and reduce the effect of the tip vortices of the blades. The duct is 15 m long and it has an edge length of 2.4 m. The computational domain is extended from approximately five rotor diameters upwind to 8 rotor diameters downwind of the turbine.

The 3-D mesh with $12,000,000$ computational cells was the extrusion of the 2-D coarse mesh with spanwise step size of $c/10$. The geometry was divided into two zones, i.e. stationary and rotating. The rotor was inserted in a rotating zone forming a sliding interface with the rest of the computational domain that was set to be stationary.

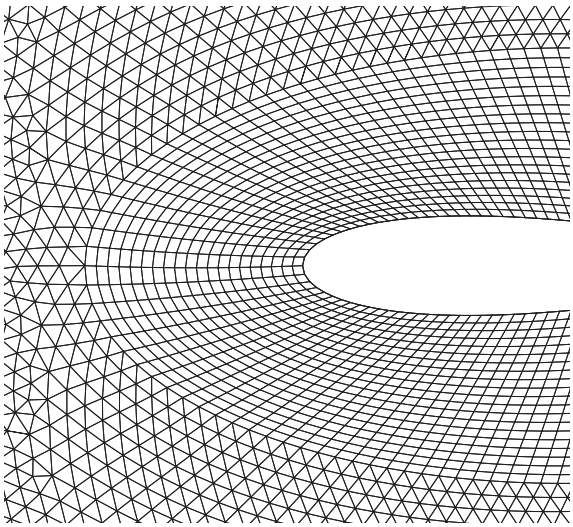

Figure 8: Mesh scheme around the NACA 0018 blade profile

Figure (8) illustrates the mesh scheme around the NACA 0018 blades. The mesh was identical for all blades. The blades were treated as walls with no-slip condition. The M18 model was modelled by the standard wall function. Thus, for valid results in the near-wall region, the non-dimensionalized distance from the wall, y^+, should be higher than 30. This requirement was satisfied by analysis of the mesh around the blades that was performed by running the simulation for different grid spacing near the blades.

Fig. (6) shows the scaled top view of the rotor. The dashed line connecting the rotor center to blade 1 represents the zero position of the azimuth angle, θ when the free-stream flow is co-directional with positive y-axis. The direction of the rotation of the rotor is counter clockwise.

3.3.3 M22 model

Unlike the previous models i.e. the M23 and M18 geometries, the M22 model is a 3-bladed wind turbine with NACA 0022 blade profile. The rotor geometry of the M22 model is from Danao [2]. The rotor radius and chord size are $R = 0.35$ m and $C = 0.04$ m, respectively, giving $\sigma = 0.34$. The computational domain is extended from 3 rotor diameters upwind to 7 rotor diameters downwind of the turbine.

Two different mesh sizes of coarse (1 million cells) and fine (2.5 million cells) were used for this study. The mesh scheme around the blades was identical to that used for the M18 model. The geometry was divided into two zones, i.e. a stationary zone and a rotating plane. The rotor was inserted in a rotating plane forming a sliding interface with the rest of the computational domain that was set to be stationary.

The blades were considered as walls with no-slip condition. In order to capture

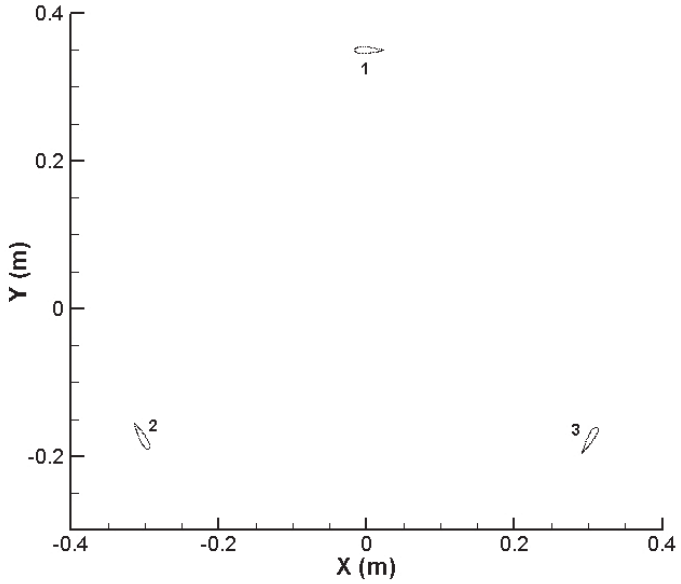

Figure 9: Top view of the rotor with NACA 0022 blade profile (scaled)

the viscous sublayer in the near-wall regions of the flow, the value of the non-dimensionalized distance from the wall, $y+$, was kept lower than 1.2 for all blades.

3.4 Computational Set Up

The commercial finite volume CFD code ANSYS® FLUENT® release 12.1.4 was used for the simulations.

The boundary conditions of pressure inlet and pressure outlet were applied for inlet and outlet of the computational domain, respectively. The working fluid was air that was treated as an incompressible fluid of density $\rho = 1.225$ with ideal-gas properties. Turbulence intensity, I, was set to be as low as 0.01 at the inlet. This modification was applied to reduce the effect of the turbulence intensity of the wind on the turbulence generated in the wake of the rotor. Temperature at both inlet and outlet was set at $26°C$. In order to eliminate the effect of the boundary layer along the side walls of the non-ducted VAWTs on the mean flow, the side boundaries were considered as walls with slip condition. The angular velocity of the rotor was set to be at a fixed value for each simulation from time zero.

Table (1) presents the values of the relaxation factors used for the simulation. The convergence rate that will be discussed further in the text was less than or equal to $1e-6$ for all of the governing equation. Therefore, the relaxation factors were kept at their default values.

Table 1: Relaxation factors for the simularion

Parameter	Relaxation Factor
pressure	0.3
momentum	0.7
turbulence kinetic energy	0.8
turbulence dissipation rate	0.8
turbulent viscosity	1

3.4.1 M18 Model

The simulation of the 3-D M18 model was undertaken by two state-of-the-art models of turbulence i.e. Spalart-Allmaras and RNG $k-\varepsilon$, discussed formerly. In order to evaluate the turbulence models under similar initial conditions, the computational set up was the same for both of the turbulence models. The simulations were performed by parallel computing on a minimum of 32 computational nodes. Each of the four simulations was performed for 15 days of physical time. First-order implicit transient formulation was used for the simulation. The pressure and velocity were coupled with the SIMPLE scheme. Time step sizes of $0.001s$ and $0.0005s$ were used for time discretization. A unidirectional inlet wind velocity of $V = 14$ m/s was required for the simulation. This velocity was achieved by a pressure difference of 5 kPa between the inlet having atmospheric pressure and the outlet of the duct. The near-wall regions of the flow was modelled by standard wall function available in FLUENT®.

In order to study the flow properties in the wake, the M18 model was analyzed using a 2-D geometry as well. The software used to generate and study the model were identical for both 3-D and 2-D models. Computational set up was similar to that of the 3-D model. Nevertheless, both first-order and second-order implicit transient formulations were used for the simulation of the 2-D model. The objective was to investigate the effect of the order of accuracy on the torque output and on the wake.

3.4.2 M23 Model

The simulation was undertaken by the state-of-the-art model of turbulence i.e. RNG $k-\varepsilon$ model discussed formerly. Second-order implicit transient formulation was used for the simulation. The spatial discretization was least squares cell based

for gradient. Pressure had a second-order spatial discretization. Momentum, turbulence kinetic energy, and turbulence dissipation rate were modelled based on second-order upwind scheme. Time step sizes of $0.0001s$ and $0.00005s$ were used for time discretization. This time step size was obtained from the formerly-discussed formulation for calculation of the non-dimensional time step size.

The boundary conditions of pressure inlet and pressure outlet were applied for inlet and outlet of the computational domain, respectively. The flow was induced by a pressure difference of 20 Pa between the inlet having atmospheric pressure and the outlet of the geometry. The angular velocity of the rotor was set to be $\omega = 280$ rpm.

3.4.3 M22 Model

The RNG $k - \varepsilon$ turbulence model with second-order implicit transient formulation was used for the simulation. The spatial discretization was least squares cell based for gradient. Pressure had a second-order spatial discretization. Momentum, turbulence kinetic energy, and turbulence dissipation rate were modelled based on second-order upwind scheme. Time step size was $0.00005s$ for time discretization.

The inlet wind velocity was $V = 7$ m/s. The aerodynamics of rotor was analysed at $\lambda = 4$. The near-wall region of the flow was modelled by enhanced wall function of the RNG $k - \varepsilon$ turbulence model available in FLUENT®.

3.4.4 Level of Convergence of the Solution

Table (2) presents the value of the required residuals for convergence. The continuity equation shows the highest residual with a value of $1E{-}6$. The residuals indicate an acceptable level of convergence of the solution.

Table 2: Residuals for the model equations

Equation	Residual
continuity	$1E-6$
x-velocity	$1E-10$
y-velocity	$1E-8$
k	$1E-11$
ε	$1E-9$

3.4.5 Non-Dimensionalized Distance From the Wall

Simulations were undertaken with no-slip boundary condition along the blades. In order to capture the viscous sublayer in the near-wall regions of the flow, the value of the non-dimensionalized distance from the wall, $y+$, should not exceed unity. The value of $y+$ for the M23 model blade is plotted in figure 10. As illustrated, y^+ is reported less than 1.1. High values of $y+$ correspond to the grids neighbouring the leading edge of the blades where the value of velocity gradient is higher. Accordingly, $y+$ decreases with increasing distance from the leading edge towards the trailing edge of the blades where $y+$ is approximately null. Figure 11 illustrates the values of y^+ for the NACA 0022 blade profile used in M22 model. It can be safely argued that the viscous sublayer is fully captured with $y^+ < 1.1$.

In order to overcome the computational expense related to the high-density mesh around the blades, the near-wall regions of the flow in 3-D M18 geometry were modelled by the standard wall function available in $FLUENT^{\circ}$. Thus, in order to obtain computationally valid data in the near-wall areas of the flow, the value of the non-dimensionalized distance from the wall, $y+$, should be greater than 30 and less than 300 [17]. The values of $y+$ from RNG $k-\varepsilon$ and S-A models are plotted in figure 12. As expected, values of $y+$ are similar. This confirms that both turbulence models use identical wall functions. High values of $y+$ correspond

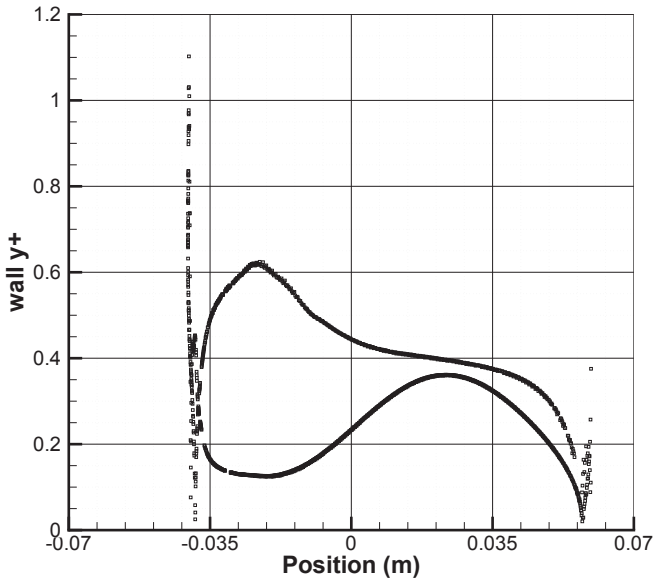

Figure 10: wall y^+ for S1223 blade profile

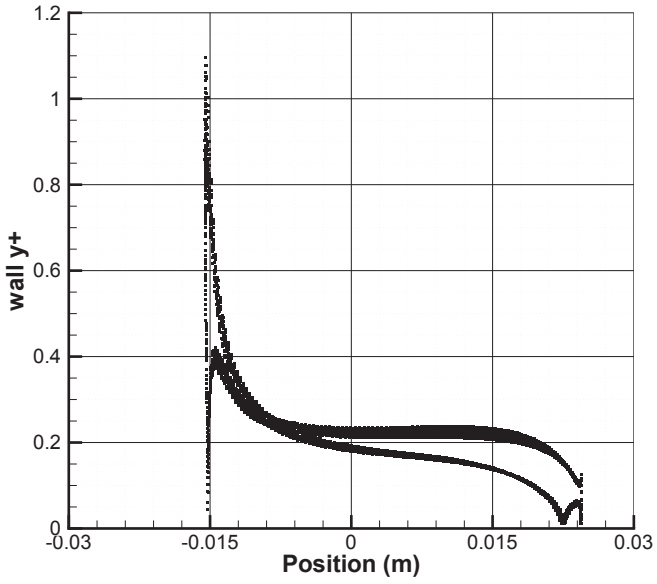

Figure 11: wall y^+ for NACA 0022 blade profile

to the leading edge of the blade where the value of velocity gradient is higher.

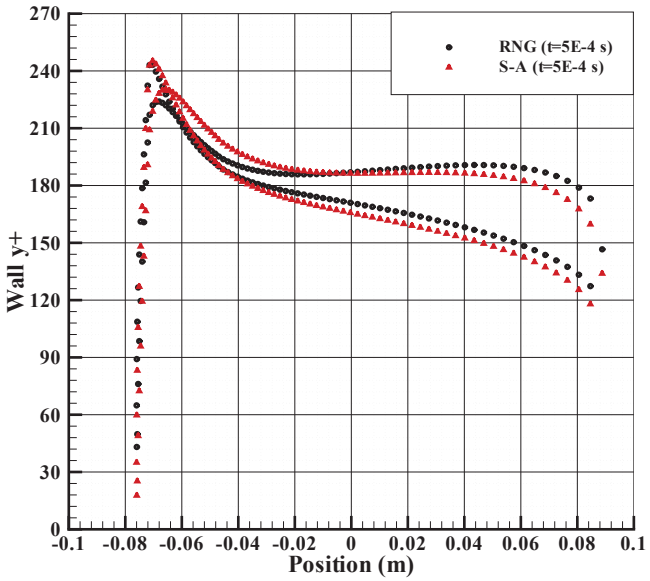

Figure 12: wall y^+ for NACA 0018 blade profile obtained by S-A and RNG $k-\varepsilon$ models (3-D geometry)

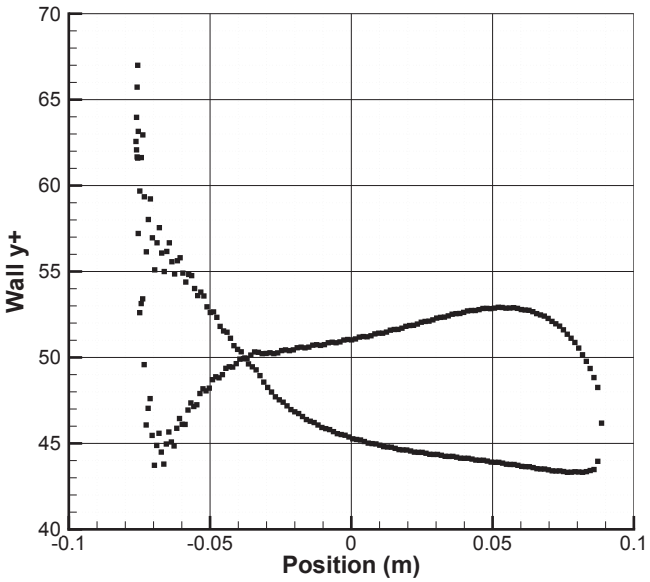

Figure 13: wall y^+ for NACA 0018 blade profile (2-D geometry)

In order to have an identical near-wall treatment for the 2-D and 3-D M18 geometries, the 2-D geometry was modelled with standard wall function around the blades as well. Figure 13 illustrates y^+ versus position for the 2-D model for which $42 < y^+ < 67$. This range is valid for use of the standard wall function.

3.5 Time Step

The aerodynamics of the VAWT is highly complex due to strong unsteadiness and dynamic-stall. Thus, time step size is of crucial importance in the CFD analysis of VAWTs. The time step for a specific mesh was determined based on the maximum relative velocity of the free-stream wind with respect to the rotating blade, V_{rel}, during the rotation of the rotor. Figure 14 shows the location of the blade at which V_{rel} reaches its maximum. This location corresponds to $\theta = 0°$.

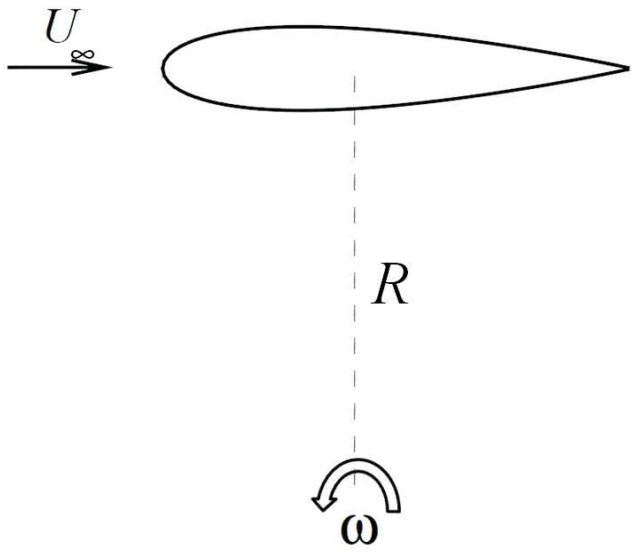

Figure 14: Position of the blade with respect to the free-stream wind at which V_{rel} reaches its maximum

The time step size is obtained according to:

$$dt = \frac{dx}{R\omega + U_\infty}$$

where dx is the chord-wise mesh step size around the blade. This approximation gives a time step size of approximately $dt = 0.0001$ s for the 2-D M18 and M23 models at $\lambda = 1.5$ or lower. Nevertheless, the M22 model simulated at $\lambda = 4$ requires a smaller time step size of approximately $dt = 0.00005$. The above formula determines the minimum time step required for the simulation at $\theta = 0°$ at which V_{rel} reaches its maximum. The maximum torque output of the VAWTs with S1223 or the conventional symmetric blade profiles including NACA 0018 and NACA 0022, is generated in the azimuthal range of $50° < \theta < 90°$. Analysis of the torque generated by the 3-D M18 model that is discussed further in the text was performed by larger time step sizes of 0.0005 s and even 0.001 s from which highly similar values of T_b were achieved.

Sørensen and Michelsen [18] analyzed the temporal convergence of the solution of flow over a 2-D flat plate placed perpendicular to the free-stream velocity vector. The aim was to determine the time step size for prediction of drag at high angle of attack for computational analysis of HAWTs using $k - \omega$ turbulence model. The observed quantity was the drag force coefficient on the plate. The corresponding authors suggest a minimum non-dimensional time step size of $dtU_\infty/C = 0.01$ for relative temporal convergence of the computational solution. This criterion was used by Li et al. [19] for computational analysis of a single airfoil of a VAWT using large eddy simulation (LES). This approximation gives the time-step sizes of:

$$dt = 0.01\frac{C}{U_\infty} = 0.01\frac{0.1m}{6m/s} = 0.000166s$$

for the S1223 blade profile with $C = 0.1$ m and $U_\infty = 6$ m/s,

$$dt = 0.01\frac{C}{U_\infty} = 0.01\frac{0.16m}{14m/s} = 0.000114s$$

for the NACA 0018 blade profile with $C = 0.16$ m and $U_\infty = 14$ m/s, and

$$dt = 0.01\frac{C}{U_\infty} = 0.01\frac{0.04m}{7m/s} = 0.000057s$$

for the NACA 0022 blade profile with $C = 0.04$ m and $U_\infty = 7$ m/s. Therefore, the time-step sizes obtained by this formulation are higher than what was used in this study.

4 Verification and Validation

4.1 Effect of the Mesh Density on the Generated Torque

The M23 geometry was used for verification of the simulation methodology. The rotor dimensions and blade profile are identical to those used by Ji and Schluter [1]. The simulations were run for a total flow time of 2 s. During this time interval, the wake reaches a quasi-steady state. Considering an inlet velocity of 6 m/s and total domain length of 6 m, this time interval is twice the time required for the undisturbed inlet flow to reach the outlet of the domain.

In this analysis, the angular velocity of rotor and the wind speed were $\omega = 280$ rpm and $U_{rel} = 6$ m/s, respectively. This configuration results in a tip speed ration of approximately $\lambda = 1$. Figure 15 illustrates the torque output from a single blade compared with the values obtained by Ji and Schluter [1]. The results are highly comparable for $90^\circ < \theta < 180^\circ$. Nevertheless, the values of torque for $180^\circ < \theta < 270^\circ$ are considerably different. This can be attributed to the resolution of the mesh. The 3-D model of Ji and Schluter [1] incorporates 2 million cells. Neither the mesh size nor the time step size for the corresponding 2-D model were mentioned. In the comparative analysis, it was considered that the 2-D geometry has considerably less than 2 million cells. The results of the torque illustrated in figure 15 were obtained by a 2-D model with 280,000 cells.

The variation of torque shows considerable change with a higher-density mesh. Therefore, the torque obtained by Ji and Schluter [1] is subject to numerical errors occurred by low mesh density.

In order to examine the spatial convergence of the simulation, the model was investigated with 4 different mesh densities i.e. very coarse, coarse, fine, and very fine with 280,000, 1.2 millions, 2 millions, and 4 millions mesh cells, respectively.

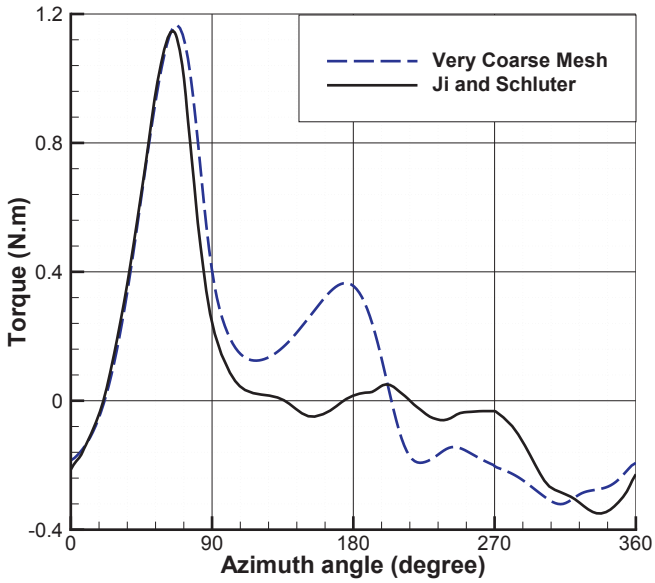

Figure 15: torque versus azimuth angle from the 2-D model with very coarse mesh compared with the values of torque obtained by Ji and Schluter [1]

The time step size was calculated based on the very fine mesh and was equal to $0.0001s$.

The torque from a single blade was analyzed to evaluate the spatial convergence. Figure 16 illustrates the torque from a single blade versus the azimuth angle. The results indicate that the finer mesh generally reports lower values of maximum torque generated by a single blade. The very coarse mesh with 280,000 computational cells gives the highest value of maximum torque. The difference between the torque obtained by the very coarse mesh and that given by the coarse mesh indicate that the very coarse mesh is unable to capture the turbulent behaviour of the flow that inversely effects the generation of torque. The torque obtained from the coarse and fine meshes are comparable. This confirms the spatial convergence of the solution.

Figure (17) illustrates that as the mesh density increases, the azimuthal lo-

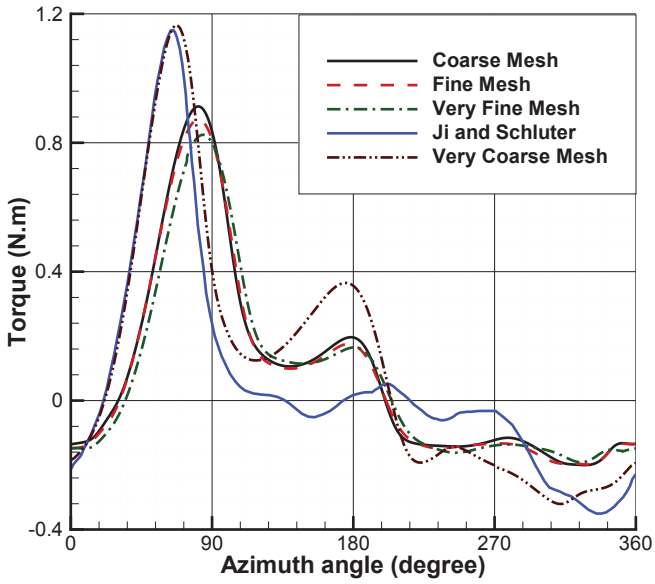

Figure 16: torque versus azimuth angle obtained by different mesh densities

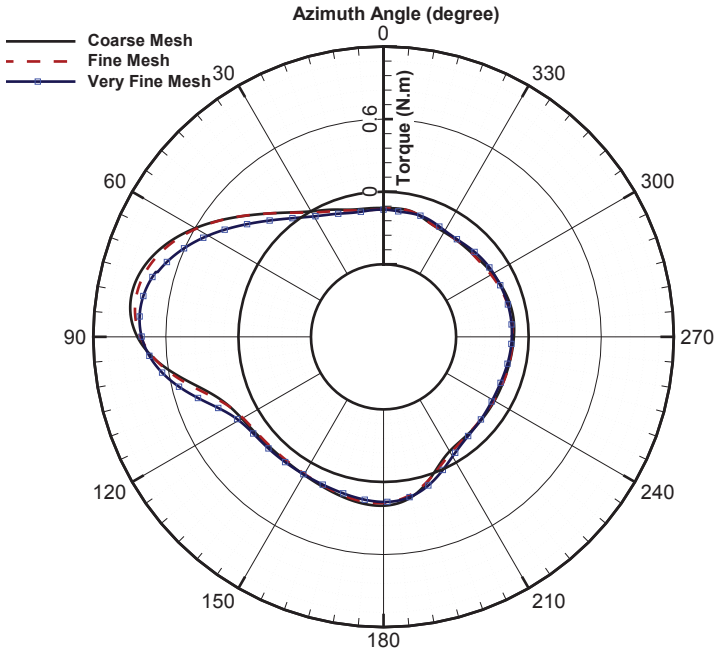

Figure 17: torque versus azimuth angle in polar system of coordinates obtained by the coarse, fine, and very fine mesh densities

cation where the maximum torque is predicted,θ_{Crit} , approaches $\theta = 90°$. The maximum value of T_b is achieved at $\theta = 84.216°$ with the very fine mesh. Nevertheless, the fine and coarse mesh densities report the maximum value of T_b at azimuthal locations of $\theta = 81.528°$ and $\theta = 81.192°$, respectively.

4.2 Effect of the Order of Accuracy on the Generated Torque

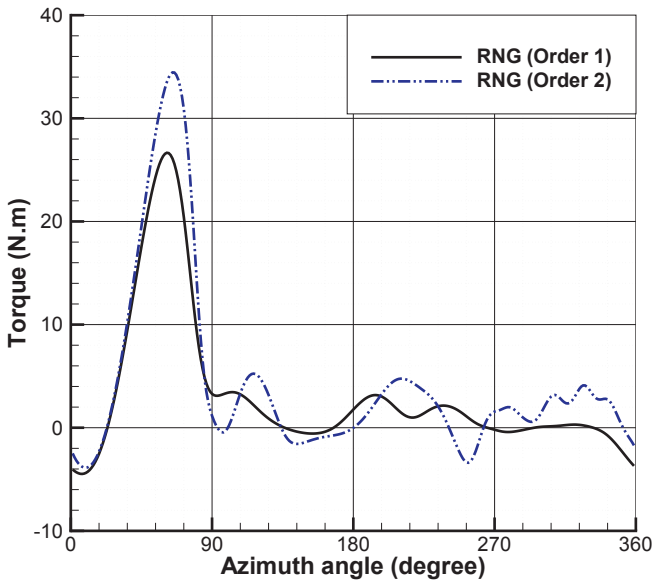

Figure 18: Torque obtained by the RNG $k-\varepsilon$ and S-A turbulence models at $\omega = 200$ rpm with first and second order accurate solvers

Figure 18 demonstrates a comparison between the values of torque obtained with first-order and second-order accuracies by the RNG $k-\varepsilon$ turbulence model. The results are from the non-ducted geometry. It is evident that the second-order-accurate solver predicts higher values of T_b. Also, higher fluctuations are reported in the values of T_b with the second-order-accurate solver.

4.3 Effect of the Order of Accuracy on the Aerodynamics of the Wake

Figure 19 demonstrates a comparison between the contours of I obtained by solvers of first-order and second-order accuracy. The levels were adjusted for optimum visualisation of the contours. Second-order-accurate solver reports higher values of I in the wake and around the blades. Both figures show highest values of I for $0 < L < R$. Nonetheless, the contours of I obtained by the second-order-accurate RNG $k - \varepsilon$ turbulence model exhibit more fluctuations in the values of I.

Figure 20 demonstrates a comparison between the contours of $\vec{\omega}$ obtained by solvers of first-order and second-order accuracy. Vorticity is reported higher by the second-order-accurate solver in the wake and around the blades. The contours of $\vec{\omega}$ obtained by the second-order-accurate RNG $k - \varepsilon$ turbulence model exhibit more fluctuations in the values of $\vec{\omega}$. Generally, the vorticity reported along the blade sides facing the axis of the rotor is positive. This is evident at the azimuthal locations of $\theta = 0^\circ$ and $\theta = 90^\circ$.

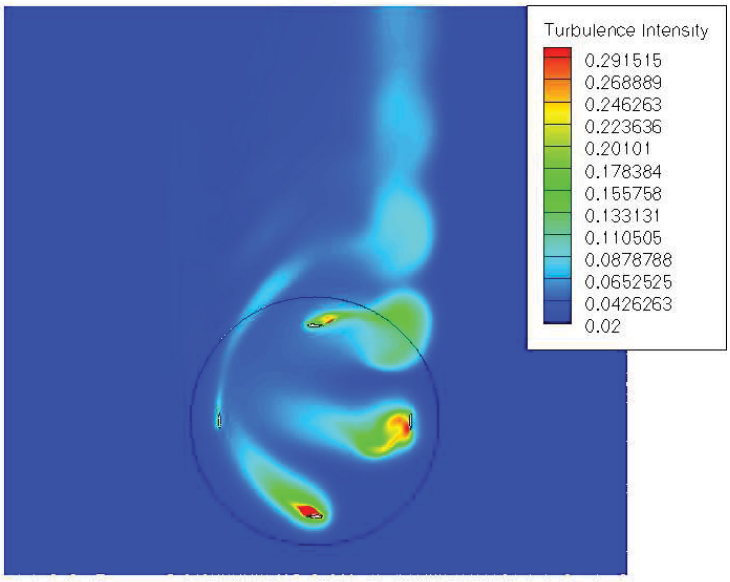

(a)

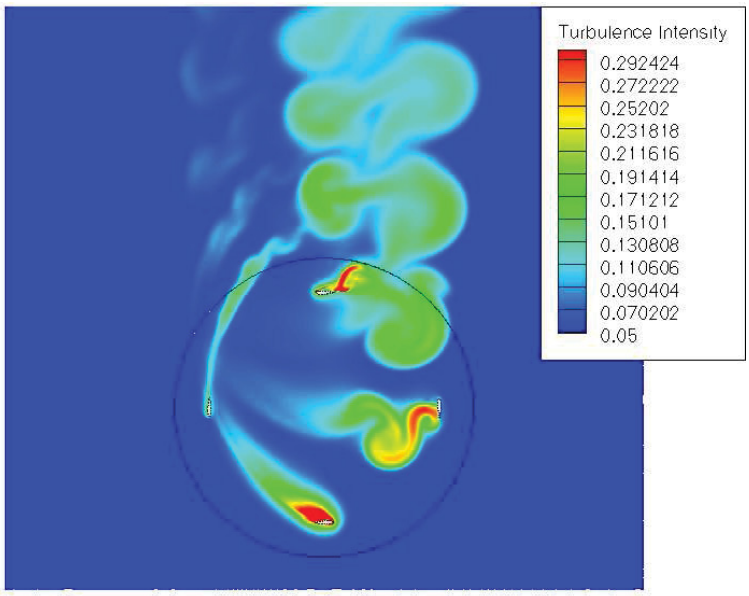

(b)

Figure 19: Contours of turbulence intensity around the rotor obtained by a) first-order-accurate and b)second-order-accurate solvers

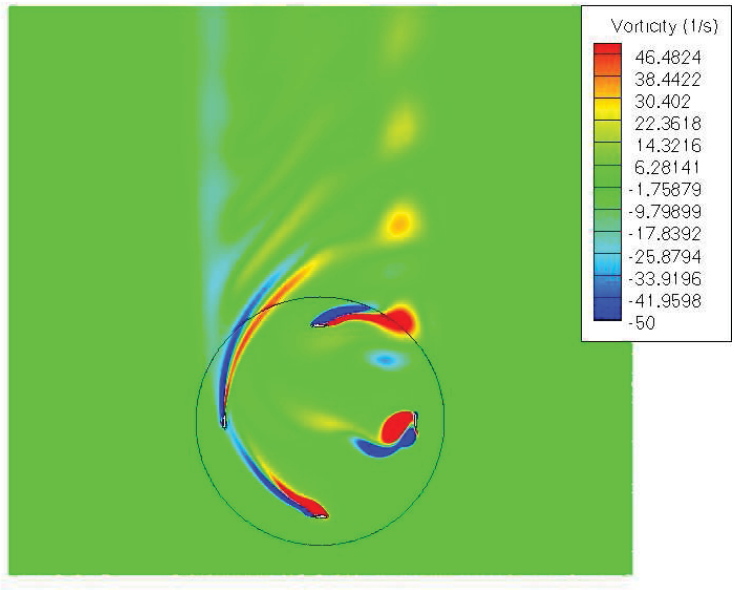

(a)

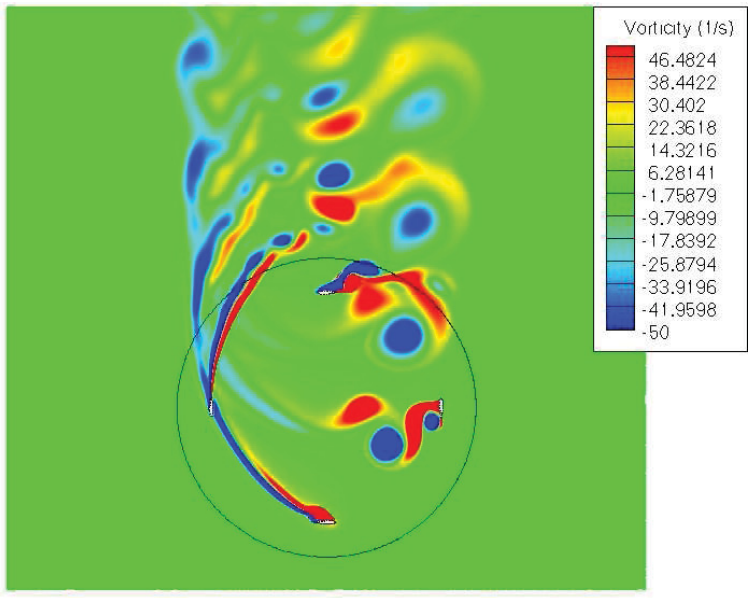

(b)

Figure 20: Contours of vorticity $(1/s)$ around the rotor obtained by a) first-order accurate and b)second-order accurate solvers

4.4 Comparison Between Numerical and Experimental Values of Power Coefficient

The M22 model was selected for validation of the methodology. The rotor dimensions and blade profile were identical to those used by Danao [2]. The numerical results obtained by the RNG $k-\varepsilon$ model and the experimental data of Danao [2] were compared at $\lambda = 4$. The simulations were run for a total flow time of 2 s. After this time interval, the wake reaches a quasi-steady state. Considering the inlet velocity of 7 m/s and total domain length of 7 m, this time interval is approximately twice the time required for the undisturbed inlet flow to reach the outlet of the domain.

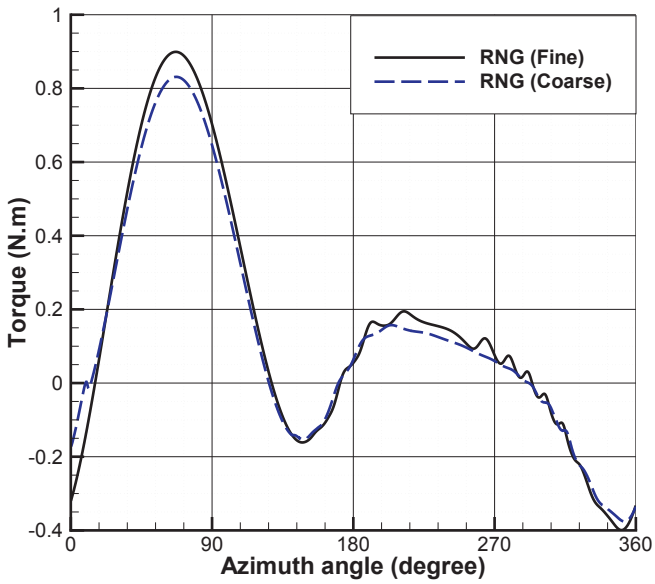

Figure 21: Torque generated by the M22 model at $\lambda = 4$

Figure 21 illustrates the values of T_b generated by the M22 model at $\lambda = 4$. The highest values of T_b are reported in the azimuthal range of $0° < \theta < 90°$ with its maximum at $\theta_{Crit} = 67°$. Torque becomes negative in the second quadrant

and increases to positive values for $180° < \theta < 270°$. In the last quarter of the revolution, T_b is mainly reported negative.

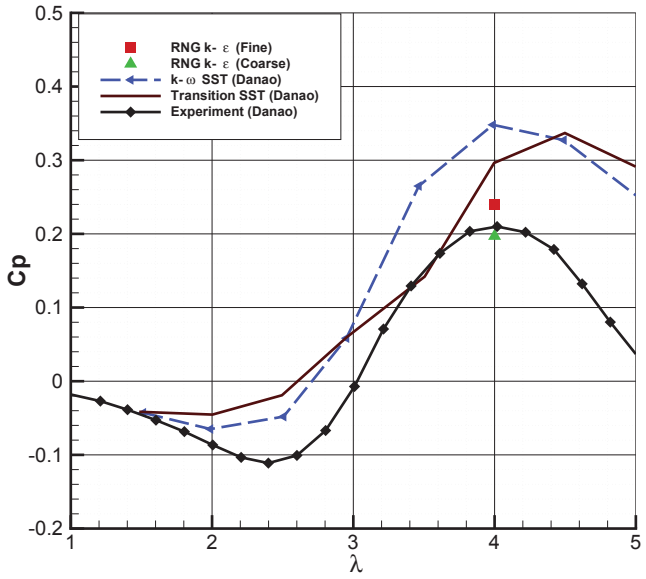

Figure 22: C_p at $\lambda = 4$ from the RNG $k - \varepsilon$ model compared with the numerical and experimental results obtained by Danao [2]

The results from the numerical analysis for estimation of C_p at different values of λ performed by Danao [2] demonstrate poor agreement with experimental data of the corresponding work (figure 22). At $\lambda = 4$ where C_p reaches its maximum value, the numerical results obtained by the Transition SST turbulence model and experimental data demonstrate up to 35% difference. The difference increases to 50% for the $k - \omega$ SST turbulence model. At $\lambda = 1.5$, the values of C_p obtained by both transition SST and $k - \omega$ SST models of turbulence are comparable with the experimental data. At higher values of λ the Transition SST model accurately predicts C_p at approximately $\lambda = 3.5$. Although the curves incorporate similar trends, the results are extensively different at other values of λ. The value of C_p obtained by the RNG $k - \varepsilon$ turbulence model in this work demonstrates close

agreement with the experimental data. This provides confidence in the results and confirms the ability of the RNG $k-\varepsilon$ turbulence model for numerical analysis of the torque generated by VAWT.

5 Results

5.1 Aerodynamics of the Wake

The wake is analysed with the fine mesh (2 million cells). Figure 23 illustrates the contours of velocity magnitude in the wake. As illustrated, the downstream velocity decreases dramatically behind the rotor. The major velocity deficit exists in approximately 2 rotor diameters after the turbine. Figure 23(a) demonstrates that the free-stream flow retrieves 50 % of its inlet velocity of 14 m/s within $2.5D$ distance in the downstream direction. The wake exhibits highly turbulent behaviour with immediate fluctuations in the values of velocity magnitude. Generally, the velocity magnitude of air within the area of the rotor is higher than that reported downstream of the turbine.

Figure 24 illustrates the velocity magnitude versus position upstream and downstream of the rotor. Figure 24(a) shows that the velocity decreases with increasing distance towards the rotor. The velocity decreases from the inlet value of 14 m/s up to approximately 11.4 m/s at $1.25D$ upstream of the rotor. In the downwind direction and in the proximity of the rotor, the velocity experiences a dramatic decrease. Figure 24(b) shows that the velocity magnitude reduces to 2.7 m/s at $2D$ downstream of the rotor. The velocity magnitude increases with increasing distance form the rotor in the downwind direction. Accordingly, the cross stream velocity profile becomes more uniform towards the outlet.

Figure 25 illustrates the contours of turbulence intensity, I. Figure 25(a) shows that turbulence intensity decreases in the wake with increasing distance from the rotor in the downstream direction. The contours of I illustrate sinusoidal and periodic trend near the outlet of the computational domain. The highest values of I are reported around the blades, specifically at $\theta = 180^\circ$ and $\theta = 270^\circ$ (figure

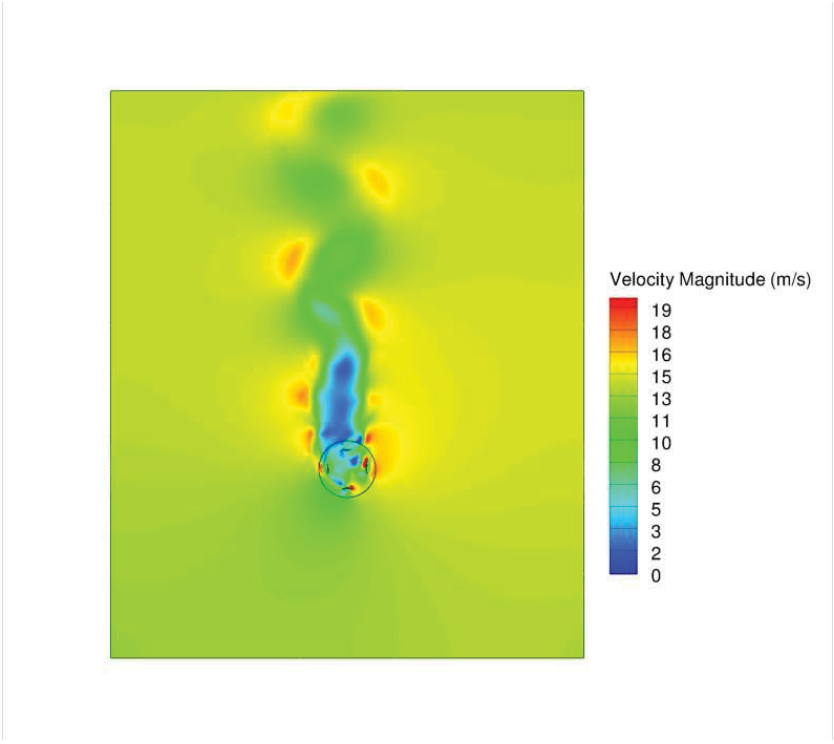

(a)

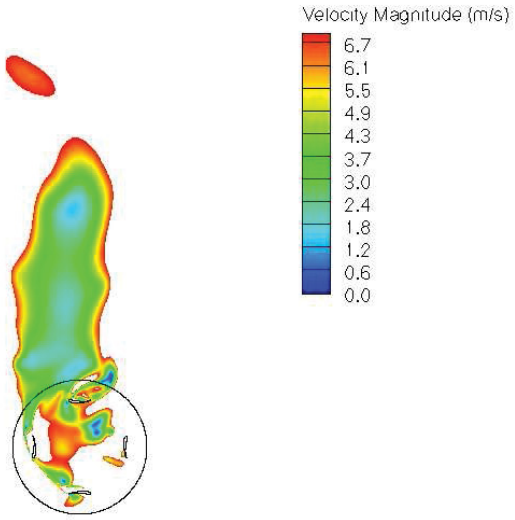

(b)

Figure 23: Contours of velocity magnitude (m/s) a) in the entire domain and b) around the rotor

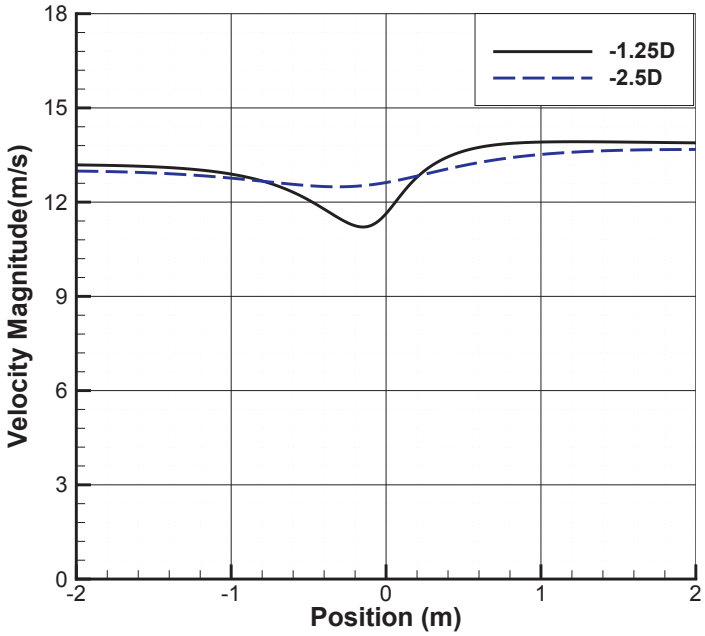

(a)

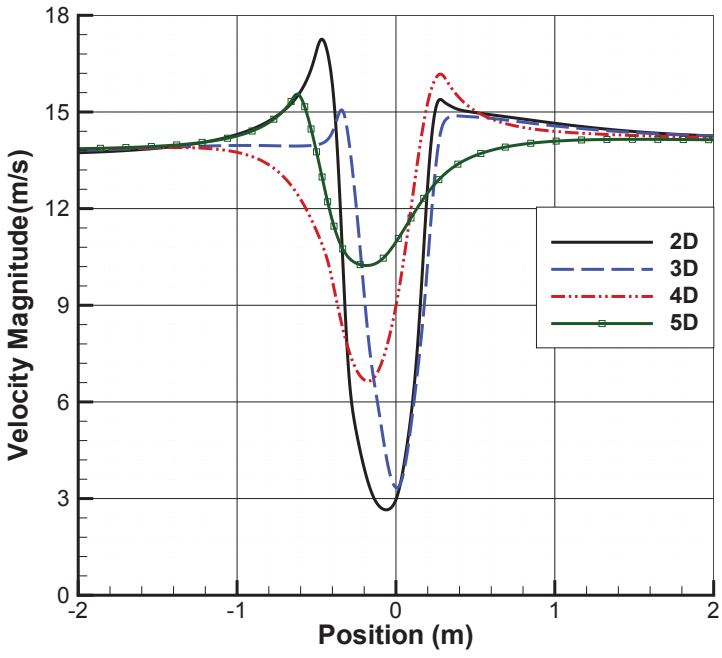

(b)

Figure 24: Velocity magnitude (m/s) versus position (m) at a) upstream and b)downstream of the rotor

25(b)).

Figure 26 illustrates I versus lateral position from $1D$ to $10D$ downstream of the rotor. As demonstrated in figure 26(a), up to $I = 0.2$ is reported at $1.25D$ downstream of the rotor. At $2D$, the intensity decreases considerably for $-R < L < R$. Generally, the highest intensity is reported along $0 < L < R$. Figure 26(b) shows the decrease of I after $5D$ downstream of the rotor. At the cross stream position of $10D$, no more than 0.07 turbulence intensity is reported.

Figure 27 illustrates the contours of vorticity, $\vec{\omega}$. Highest values of $\vec{\omega}$ are reported within the rotor. Up to $\vec{\omega} = 1000$ 1/s is reported around the blades. As illustrated, contours of $\vec{\omega}$ demonstrate a dissipative pattern. The value of $\vec{\omega}$ in the wake decreases with increasing distance from the rotor.

Figure 28 illustrates the contours of I in the wake for different values of λ and σ. The trace of the path of the rotor blade advected in the downstream of the rotor is visible in the wake of the M22 model. This is due to the high value of ω i.e. 80 rad/s corresponding to $\lambda = 4$. Figure 28 (b) shows that the wake in lower values of λ does not incorporate this effect. The solidity of the rotor effects the aerodynamics of the wake. A comparison between figures 28 (a), 28 (b), and 28 (c) suggests that the area-averaged value of I in the wake is higher for low-solidity rotors.

Figure 29 illustrates the contours of $\vec{\omega}$ in the wake for different values of λ and σ. Similar to the turbulence intensity at high values of λ, vorticity is reported highest along the traces of the path of the rotor blade that are advected in the downstream during rotation of the rotor. The area-averaged value of $\vec{\omega}$ in the wake is in direct relation to the solidity of the rotor. Figure 29 illustrates that the vorticity is highest in the wake of the rotor with $\sigma = 2$. Generally, independent of the values of σ and λ, $\vec{\omega}$ is reported positive and negative for $0 < L < R$ and

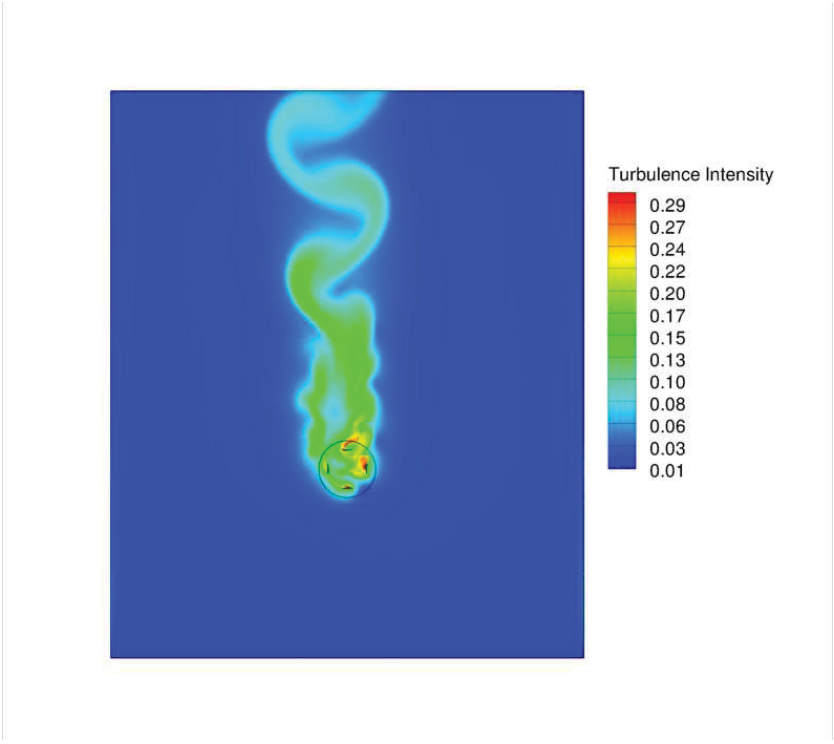

(a)

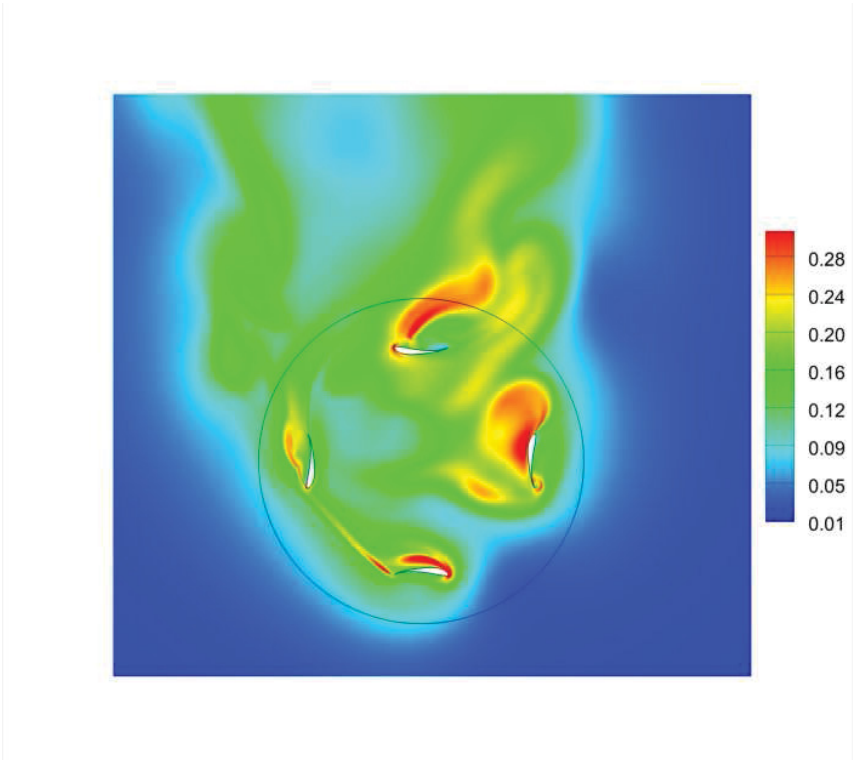

(b)

Figure 25: Contours of turbulence intensity a) in the entire domain and b) around the rotor

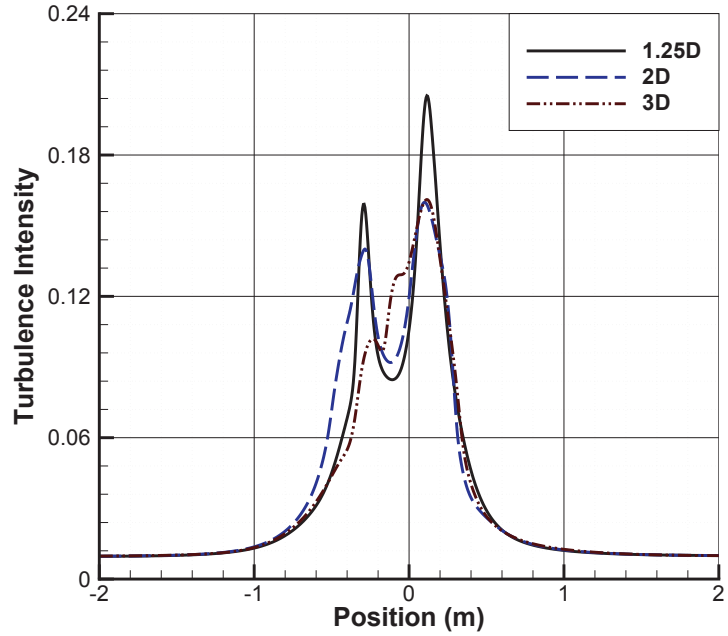

(a)

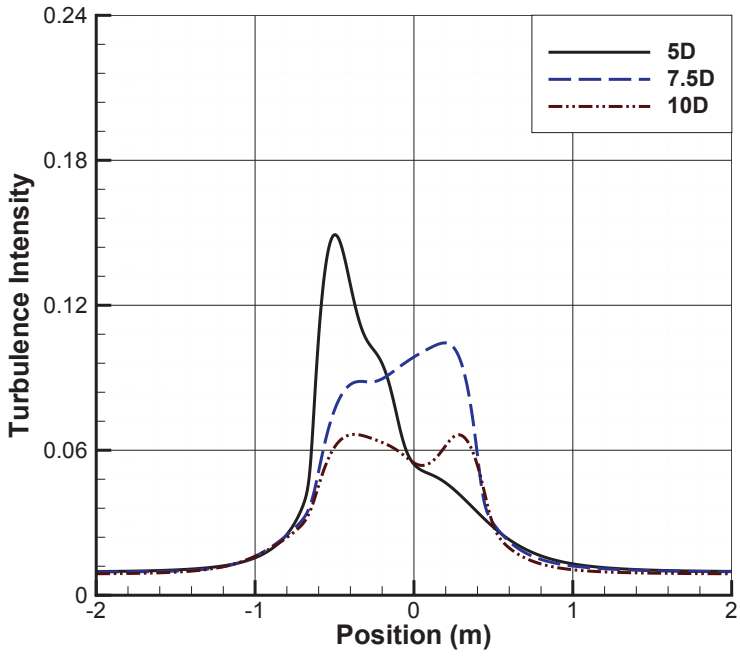

(b)

Figure 26: Turbulence intensity at a) $1D$ to $3D$ and b) $5D$ to $10D$ downstream of the rotor

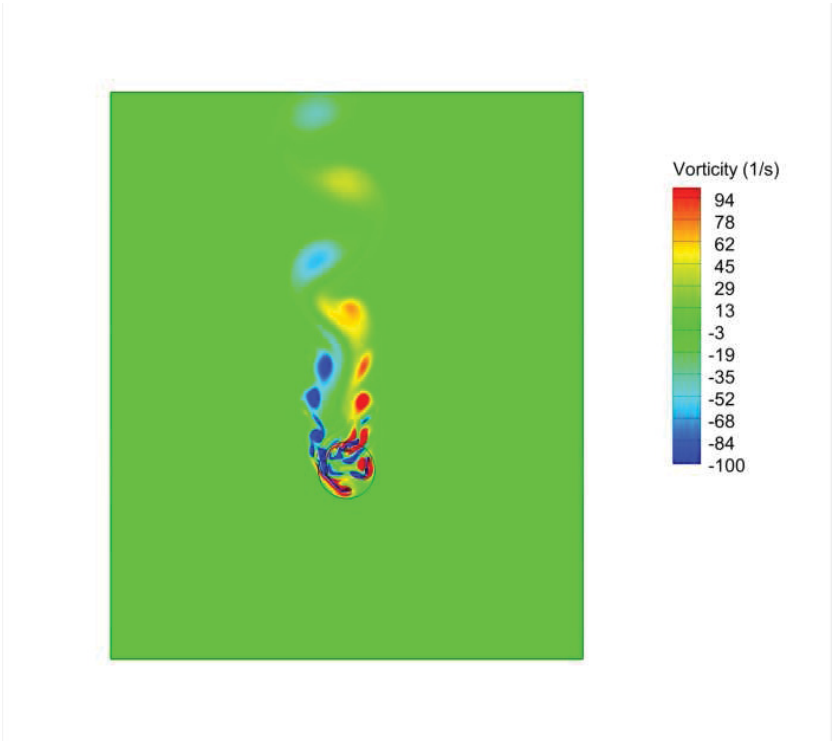

(a)

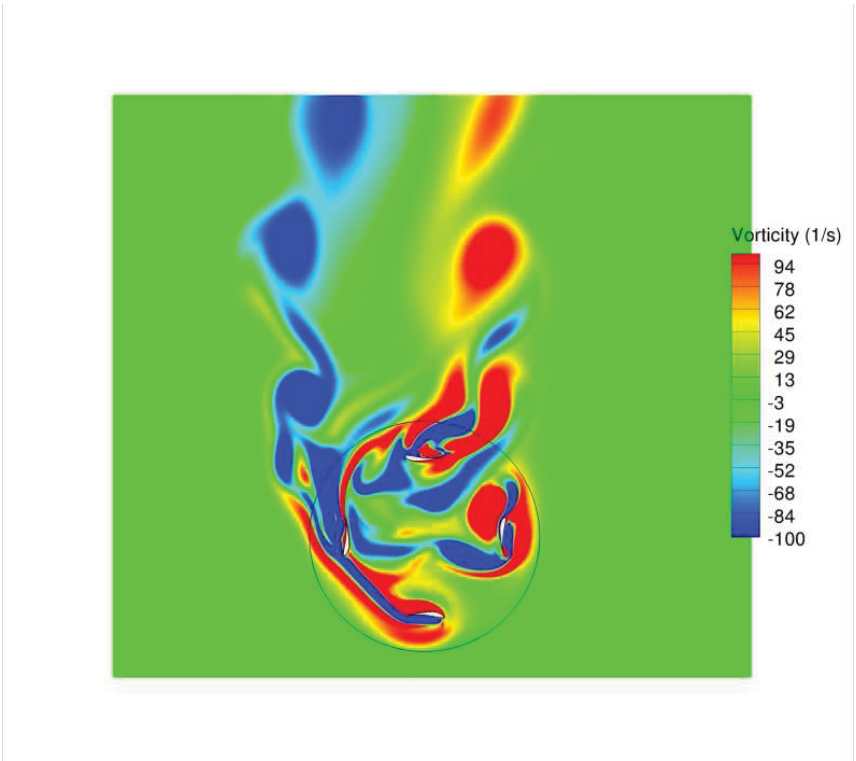

(b)

Figure 27: Contours of vorticity $(1/s)$ a) in the entire domain and b) around the rotor

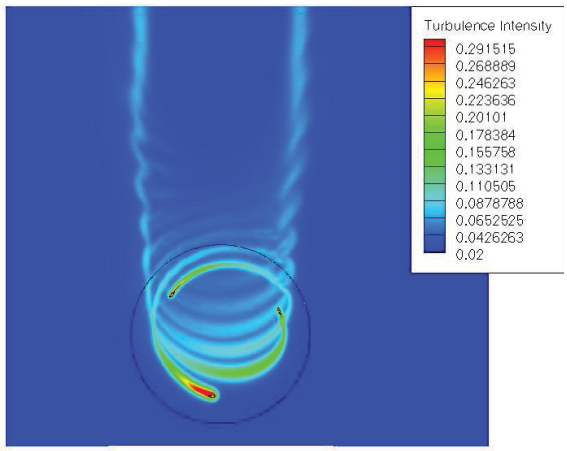

(a)

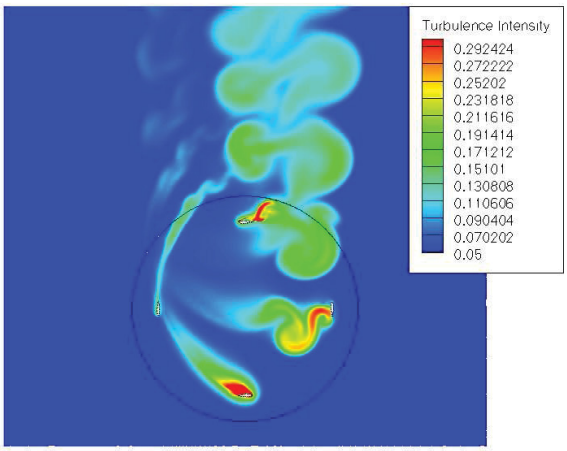

(b)

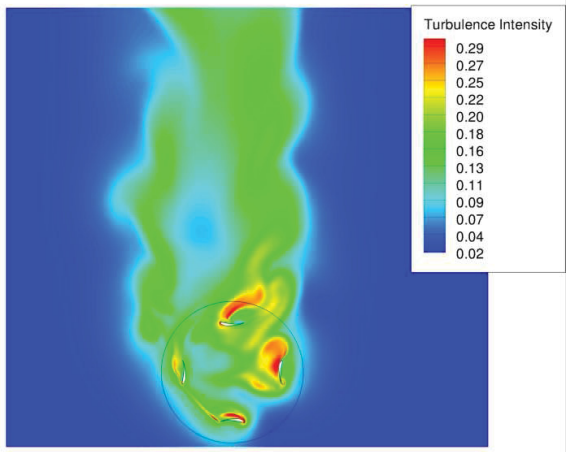

(c)

Figure 28: Contours of turbulence intensity for a)M22 model at $\lambda = 4$ and $\sigma = 0.34$, b) M18 model at $\lambda = 1.5$ and $\sigma = 0.64$, and c) M23 model at $\lambda = 1$ and $\sigma = 2$

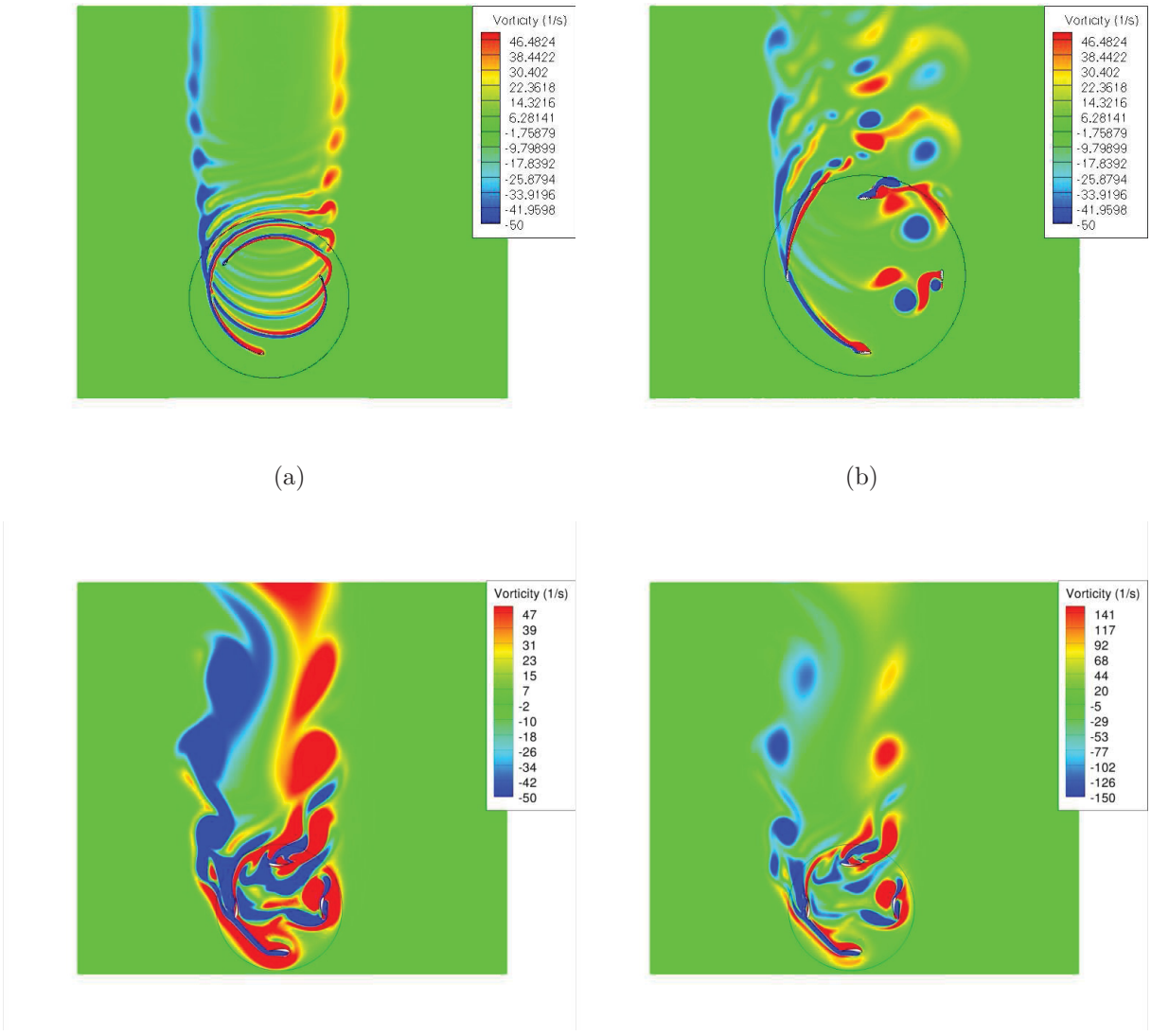

Figure 29: Contours of vorticity (1/s) for a) M22 model at $\lambda = 4$ and $\sigma = 0.34$, b) M18 model at $\lambda = 1.5$ and $\sigma = 0.64$, and c&d) M23 model at $\lambda = 1$ and $\sigma = 2$ with different contour levels

$-R < L < 0$, respectively.

5.2 Ducted VAWTs

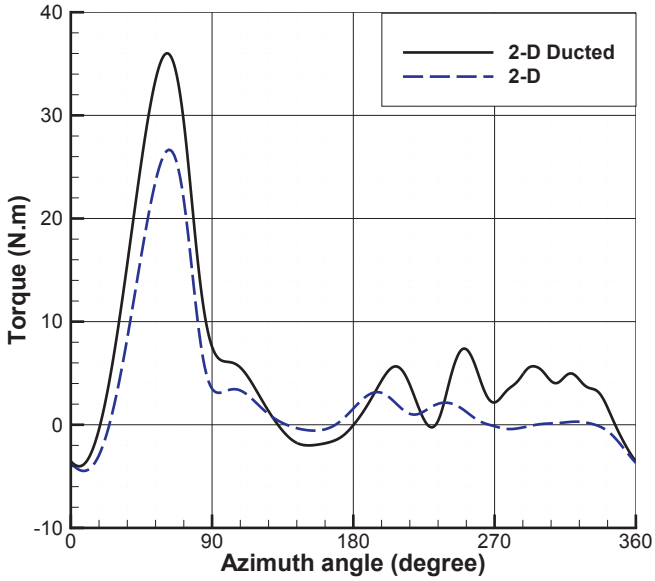

Figure 30: T_b obtained by the ducted and non-ducted 2-D models

This analysis was performed to investigate the performance of a ducted VAWT. The 2-D M18 Model was studied at rotor angular velocity of $\omega = 200$ rpm corresponding to the tip speed ratio of $\lambda = 1.5$. The mesh was coarse for both ducted and non-ducted models. The simulations were run for a total flow time of $2s$ within which the wake reaches a quasi-steady state. Considering the inlet velocity of 14 m/s and total domain length of $15m$, this time interval is approximately twice the time required for the undisturbed flow from the inlet to reach the outlet of the domain.

The simulations were undertaken with ducted and non-ducted 2-D geometries. As illustrated in figure 30, the values of torque obtained from the ducted rotor are higher than those obtained by the non-ducted turbine. Nevertheless, both

models predict a comparable trend for the variation of the torque generated by a single blade with its maximum at approximately $\theta = 60°$. This indicates that the domain walls have little effect on the variations of angle of attack. At this azimuthal location the value of T_b obtained by the ducted and non-ducted geometries demonstrate a difference of approximately 30%.

Table 3 presents the total flow time, t_t, and the number of revolutions for figures 31 and 32 in which t_t increases from top left to the bottom right figure. Figures 31 and 32 illustrate the history of development of the flow in the computational domain. For this configuration, the computational domain was initialized with zero velocity to visualize the development of the wake. Relatively lower values of velocity are reported downstream of the rotor where the wake is dominant. Velocity is higher in between the wall and the periphery of the rotor. The highest values of velocity are observed where the rotation of the rotor is in the free-stream flow direction. The value of velocity approaches its inlet value with increasing distance from the rotor in downstream direction i.e. the cross stream velocity profile becomes more uniform in the downstream towards the outlet. The changes in the velocity field are negligible after 40 revolutions. This indicates that the flow has reached a quasi-steady state.

Table 3: t_t versus the number of revolutions for figures 31 and 32

t_t (s)	number of revolutions
1.20	4
2.40	8
3.00	10
4.20	14
5.40	18
8.40	28
10.20	34
12.60	42

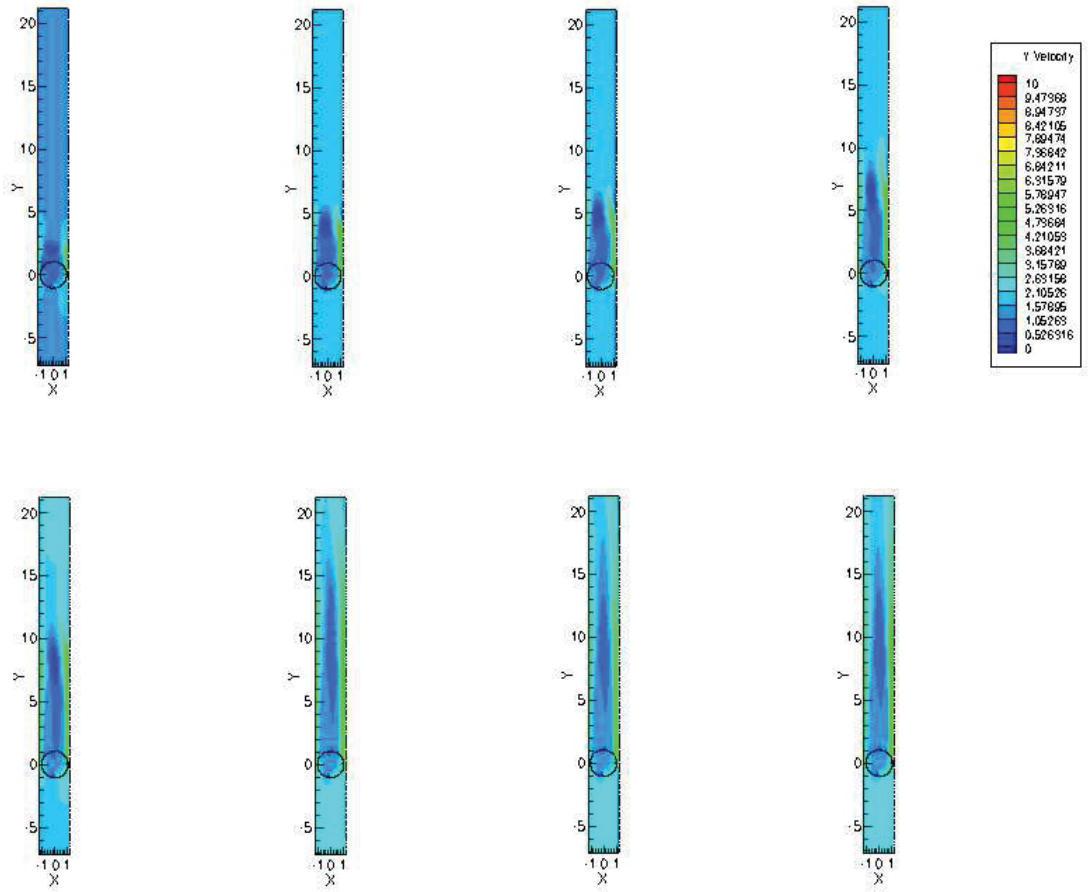

Figure 31: History of streamwise velocity component (m/s) for RNG $k-\epsilon$ model

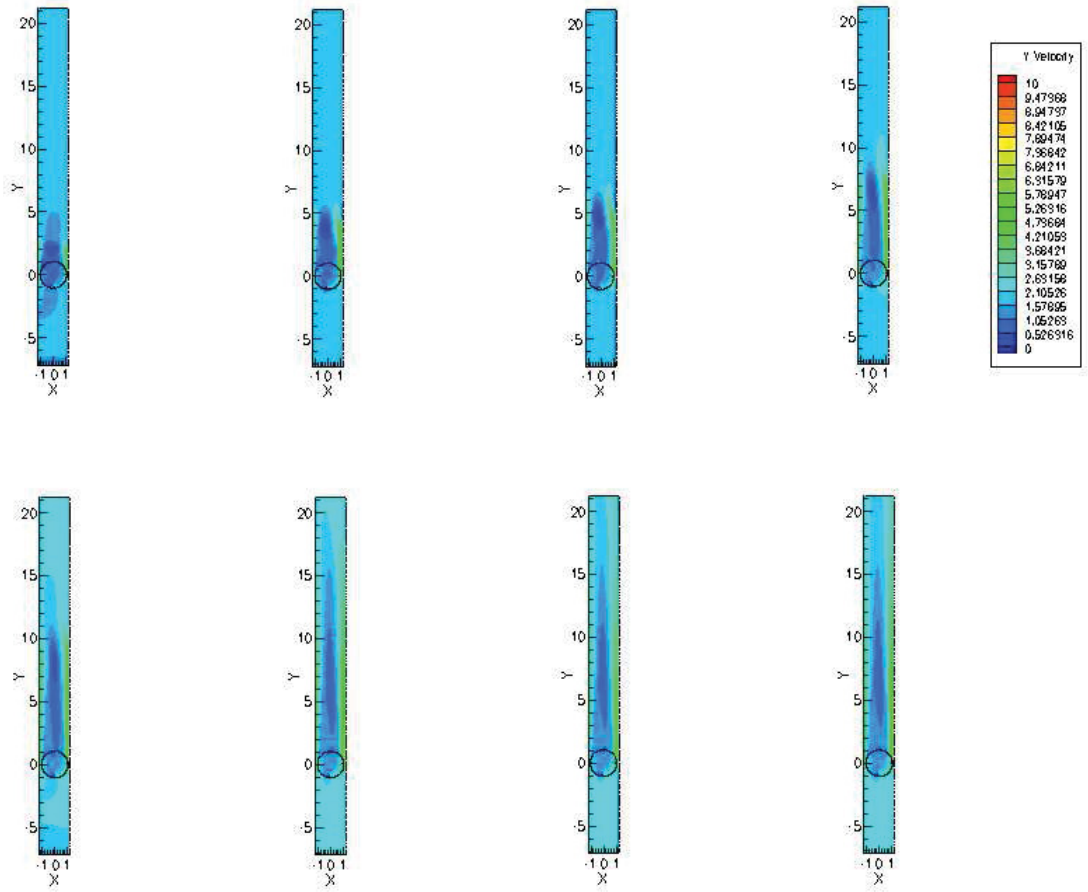

Figure 32: History of streamwise velocity component (m/s) for $S - A$ model

5.3 Comparison Between the Values of Blade Torque Obtained by RNG $k-\varepsilon$ and S-A Turbulence Models

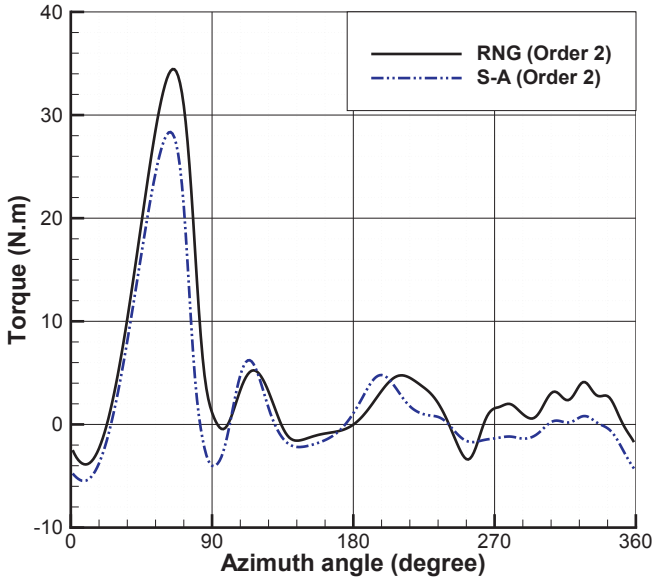

Figure 33: Torque obtained by the RNG $k-\varepsilon$ and S-A turbulence models at $\omega = 200$ rpm with first and second order accurate solvers

The results are from M18 model using the coarse mesh. Figure 33 suggests that compared to the values of torque obtained by the S-A turbulence model, the RNG $k-\varepsilon$ model predicts higher values of T_b. This is in agreement with the results obtained by the 3-D geometry that is discussed further in the text. Both graphs show approximately identical values of θ_{Crit} where the maximum T_b is achieved.

5.4 3-D Model

The 3-D M18 model is a straight-bladed extrusion of the 2-D geometry. The 3-D mesh is a straight extrusion of the 2-D coarse mesh with spanwise step size of $c/10$. Figure 34 illustrates the torque from a single blade, T_b. The highest T_b is obtained during the first 90° rotation with its peek at about $\theta = 54°$. T obtained

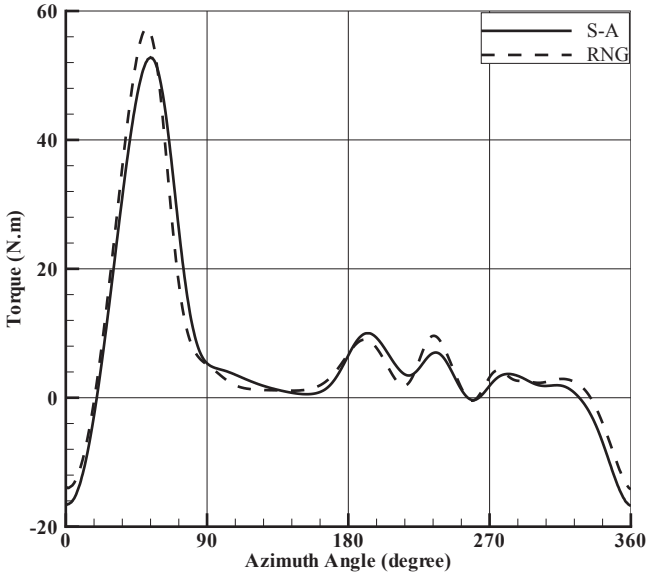

Figure 34: Torque versus azimuth angle from blade 1 obtained by S-A and RNG $k-\varepsilon$ models

by S-A and RNG $k-\varepsilon$ models is different by 7% at this azimuthal location. Between $\theta = 90°$ to $\theta = 180°$, T_b approaches zero. From $\theta = 180°$ to $\theta = 270°$, T_b fluctuates with low positive values. From $\theta = 270°$ to $\theta = 360°$, the value of T_b decreases and it becomes negative during the last 30° of the full revolution. The fluctuations in between $\theta = 180°$ and $\theta = 270°$ are mainly due to the effect of the wake of the opposite upwind blade. In comparison to the S-A model, the RNG model generally predicts higher values of T_b, particularly in the peak points where the highest lift force is achieved. The torque output from the blades in 90° azimuthal distances, experience 90° phase lag.

Figure 35 presents the accumulated or total torque, T_t, versus θ obtained by RNG $k-\varepsilon$ and S-A models using different time step sizes, dt. Figure 35(a) corresponds to the first 360° rotation of the turbine and shows the convergence history. T_t has a periodic and fluctuating trend after $\theta = 90°$. This is due to the

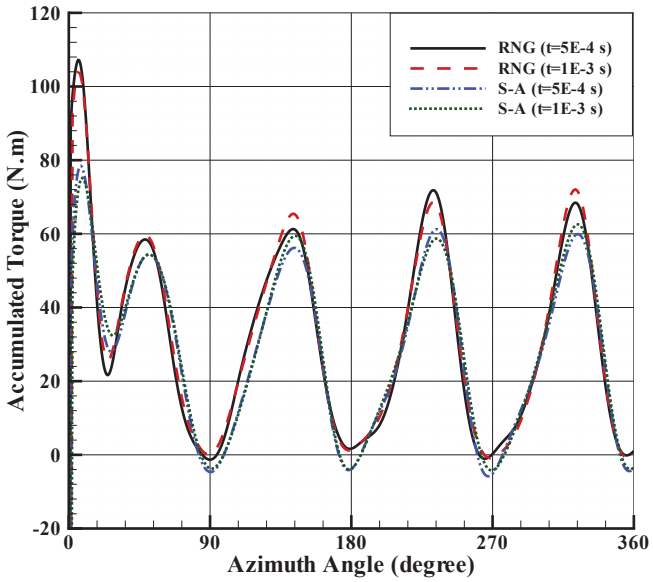

(a)

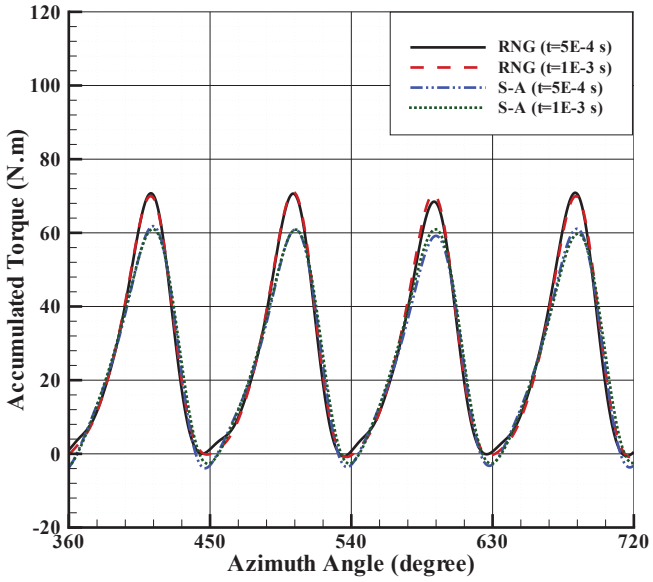

(b)

Figure 35: Accumulated torque versus accumulated azimuth angle obtained by RNG $k-\varepsilon$ and S-A models using time step sizes of 0.001 s and 0.0005 s during a) the first revolution and b) the second revolution of the rotor

fact that not all the blades experience lift at the same azimuthal location during the rotation of the rotor.

Figure 35(b) presents almost identical results obtained by t=0.001 s and t=0.0005 s during the second revolution of the rotor. This is an indication of the temporal convergence of the simulation. Due to prediction of higher values of T by the RNG $k-\varepsilon$ model, this model gives higher values of T_t. At $\theta = 230°$, the value of T_t is reported 15% higher by the RNG model.

Power coefficient, C_p, calculated from equation 13 is reported in figure 36. Due to prediction of higher T_b by the RNG model, C_p obtained by this model is generally reported higher than that given by the S-A model. In direct relation to the T_t demonstrated in figure 35, C_p follows a periodic and fluctuating trend.

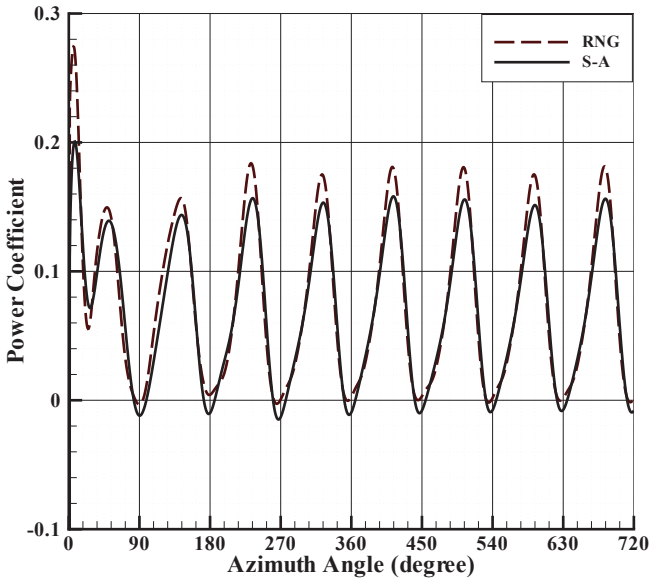

Figure 36: Power coefficient versus accumulated azimuth angle

As demonstrated in figure 37, highest values of I are reported around the blades. I is reported higher for $0 < L < R$ and it decreases with increasing distance from the rotor. I reaches a value of approximately 12% at $0.6D$ after the

rotor in the downstream direction (figure 38). The value of I decreases below 9% at 0.7D after which it mainly remains below 6%.

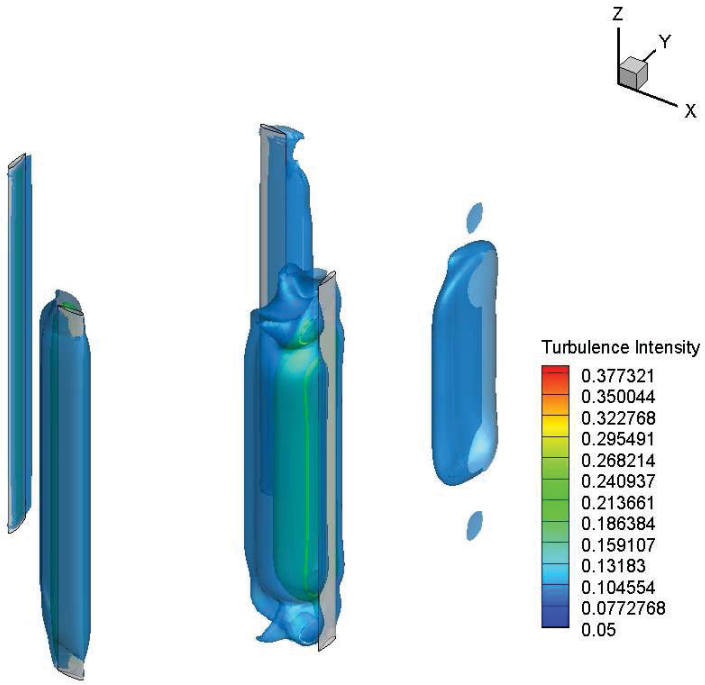

Figure 37: 3-D contours of turbulence intensity

Figure 39 illustrates the contours of velocity magnitude. Figure 39(c) illustrates the tip vortices near the rotor. The x and y components of velocity reduce to approximately zero after 0.5D distance from the rotor. Nevertheless, the contours of stream-wise component of the velocity demonstrate a non-uniform velocity distribution along the duct.

The velocity magnitude iso-surfaces in the proximity of the rotor are demonstrated in figure 40. Highest velocity in the wake is reported for $0 < L < R$ where the tangential velocity of the rotor blade is co-directional to the free-stream velocity vector at $\theta = 180°$. It can be safely argued that at the other azimuthal locations for $0 < L < R$, the tangential velocity of the rotor is not opposite to the inlet wind velocity. This is in contrast to the case of $-R < L < 0$ and confirms

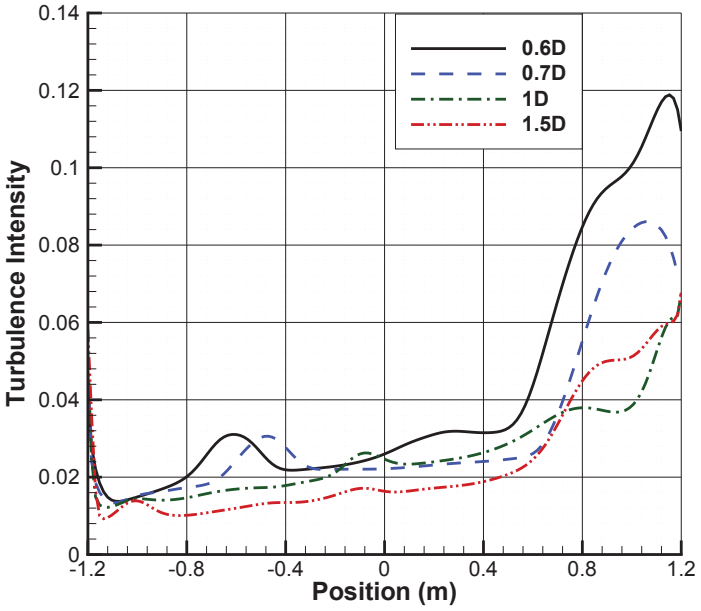

Figure 38: Turbulence intensity in the wake

the higher velocity magnitude in the near-wake for $0 < L < R$.

Figure 41 illustrates the iso-surfaces of vorticity. Mainly positive values of $\vec{\omega}$ are reported inside the area of the rotor. At this azimuthal position, the highest value of $\vec{\omega}$ in the rotor area is reported in the proximity of the rotor axis. This vorticity is generated by the upstream blade rotating from $\theta = 0°$ to $\theta = 180°$.

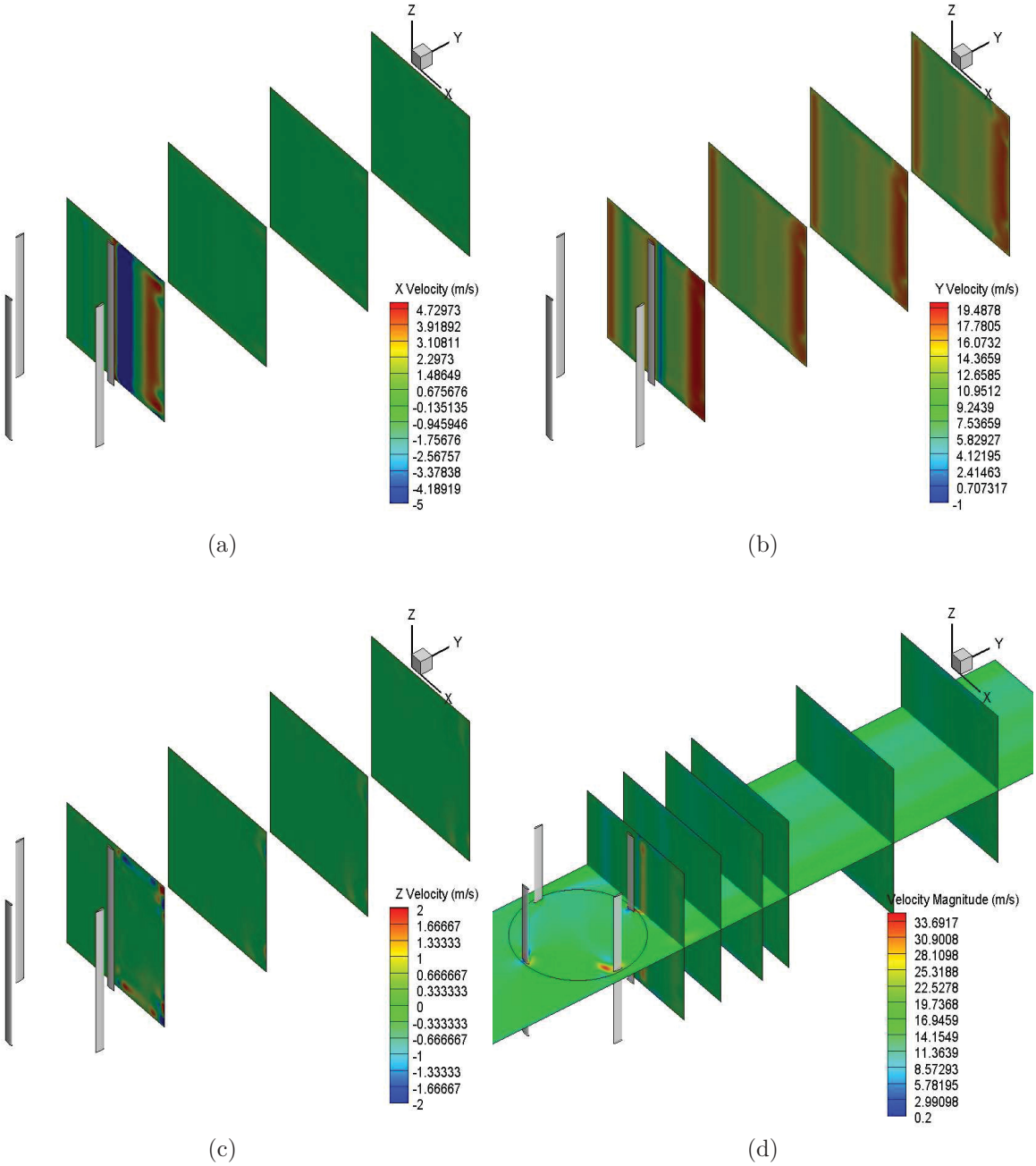

Figure 39: Contours of a) X-Velocity (m/s), b) Y-Velocity (m/s), c) Z-Velocity (m/s), and d) velocity magnitude (m/s)

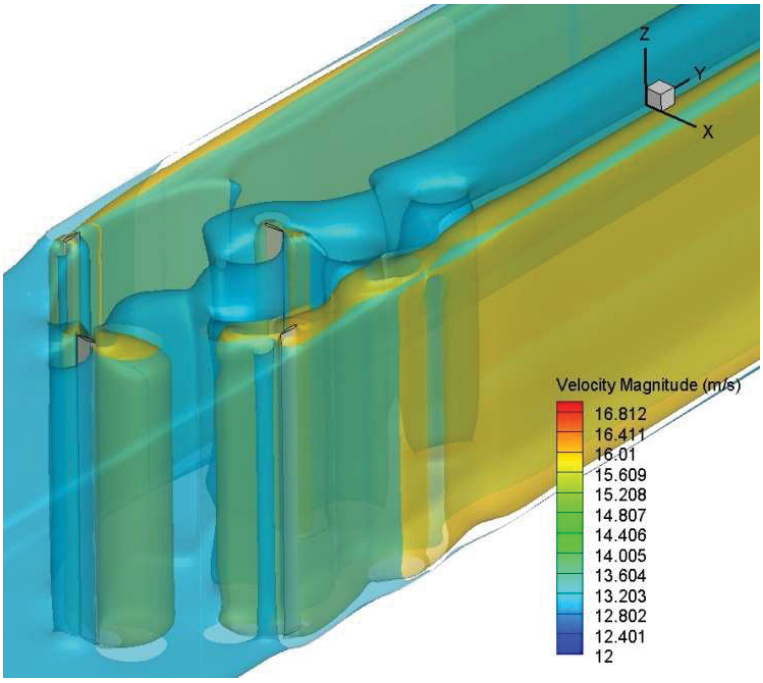

Figure 40: 3-D contours of velocity magnitude (m/s)

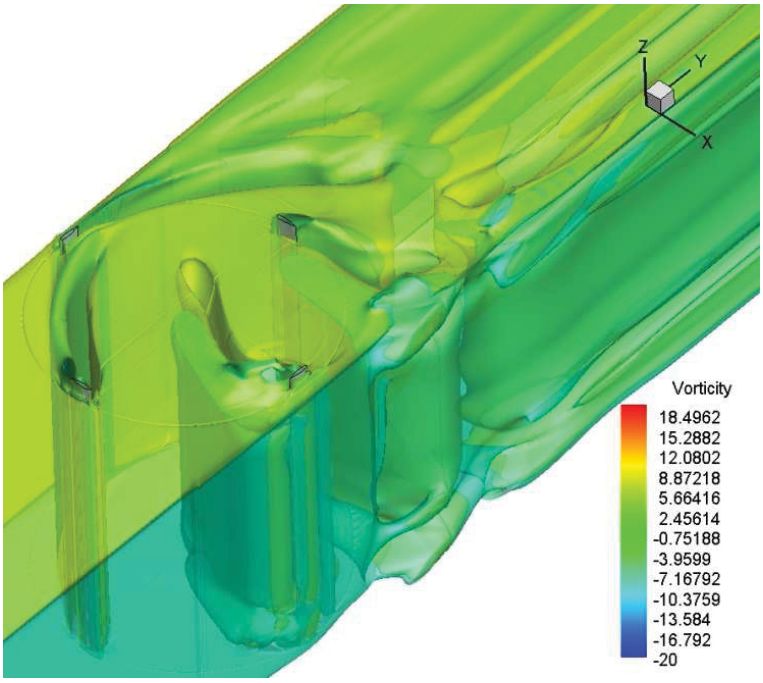

Figure 41: 3-D contours of vorticity ($1/s$)

5.5 Comparison Between the Results from 2-D and 3-D Geometries

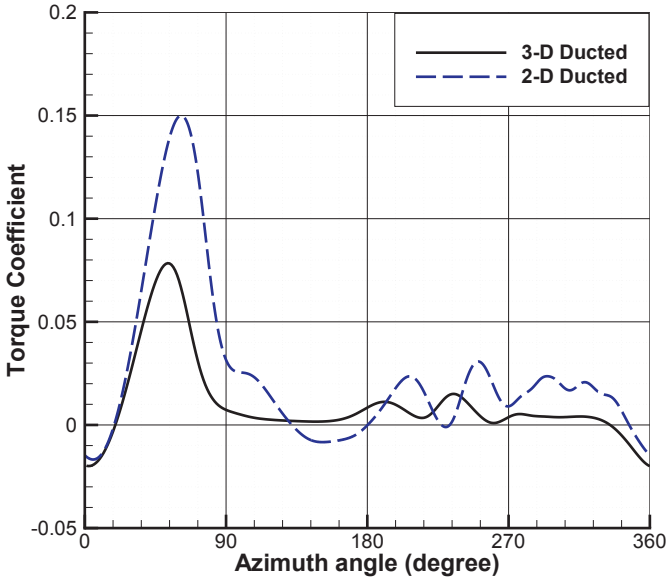

Figure 42: Torque coefficient obtained by the ducted 2-D and 3-D models at $\omega = 200$ rpm

Both models exhibit highly comparable trends for the variation of torque. The value of C_Q obtained by the 2-D model is higher than that given by the 3-D model (figure 42). This indicates that the 2-D model predicts higher values of C_p.

Both 2-D and 3-D models exhibit the same predictions for the wake of the VAWTs. The models report the highest values of $\vec{\omega}$ near the blades and in the area of the rotor. Highest velocity magnitude is reported for $0 < L < R$ by both models. The variations of turbulence intensity in the wake are highly comparable in 2-D and 3-D results.

5.6 Analysis of the Torque and the Aerodynamics of the Downstream Rotor in a Row of Two M23 VAWTs

The results presented in this section are second-order accurate in time and space with very fine (10 million) computational cells. The time step size was 0.00005 s. The M23 geometry was used for the study of a row of two VAWTs with the second rotor placed in 6 m or 15D downstream of the upwind rotor.

Figures 43 and 44 illustrate the values of U_y and U_x in the immediate upwind proximity of the downwind rotor, respectively. The values of U_y for $-R < L < 0$ are considerably lower than those reported for $0 < L < R$. This is due to the effect of the rotation of the blade in a direction mainly opposite to the free-stream flow. Figure 44 shows that in a direct relation to U_y, the values of U_x are lower for $-R < L < 0$.

Figure 45 illustrates the variation of the velocity magnitude in the downstream spacing between the two rotors. The velocity decreases in the downwind proximity of the upwind rotor after which it recovers the value of U_∞. Figure 45 demonstrates that unlike the velocity distribution in the wake of an isolated VAWT, the velocity magnitude decreases beyond 10D downstream spacing measured from the upwind rotor. This is the effect of the blockage of the free-stream flow by the downwind rotor.

Figure 46 illustrates the values of T_b at approximately $\lambda = 1$ during the 3 consecutive revolutions of the rotor. The values of T_b fluctuate in each cycle. The maximum values of T_b reported in the two consecutive revolutions are up to 40 % different. This phenomenon is the effect of the unsteady and non-unidirectional U_∞ for the downwind rotor. Figure 47 shows the fluctuations of T_t in each revolution. The trend of variation of T_t in each revolution is highly unsteady and unpredictable. It can be argued that the time-independent fluctuations of T_t and

its non-periodic behaviour can increase the vibration of the rotor.

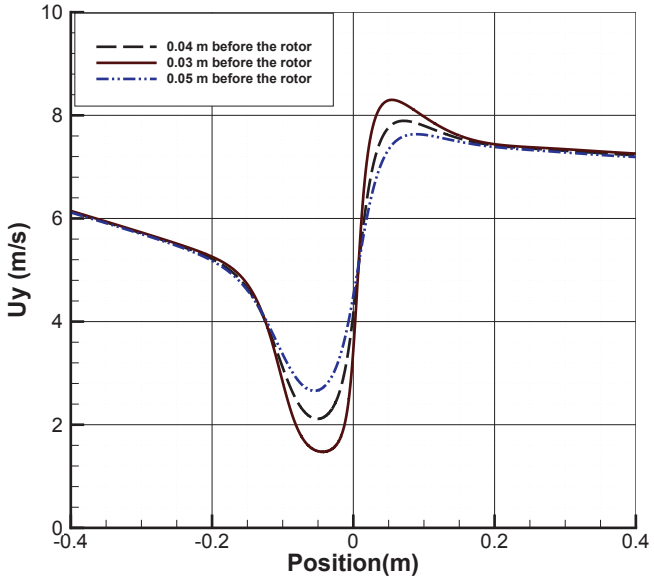

Figure 43: U_y in the immediate upwind proximity of the downwind rotor

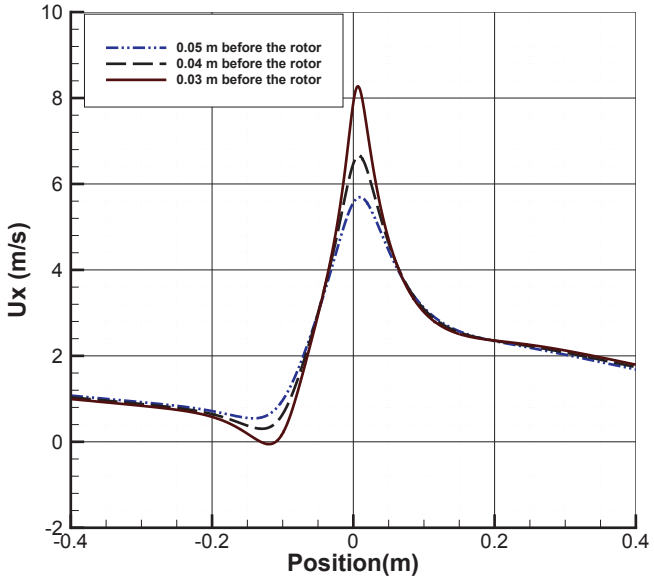

Figure 44: U_x in the immediate upwind proximity of the downwind rotor

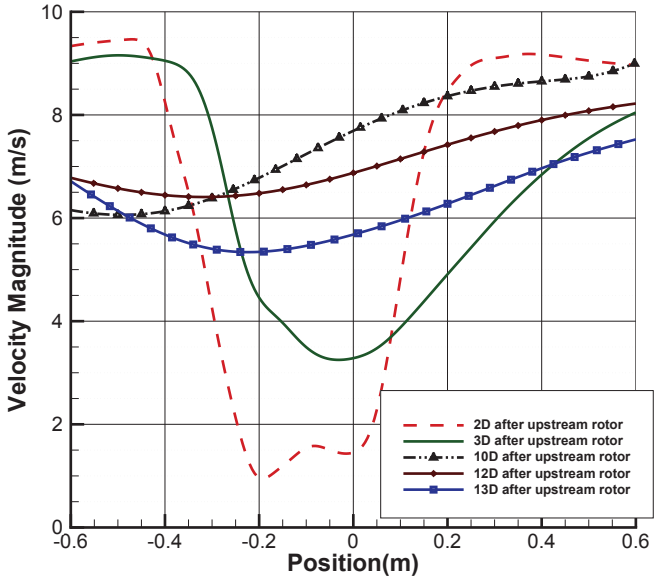

Figure 45: Velocity magnitude versus cross-stream position in the spacing between the rotors

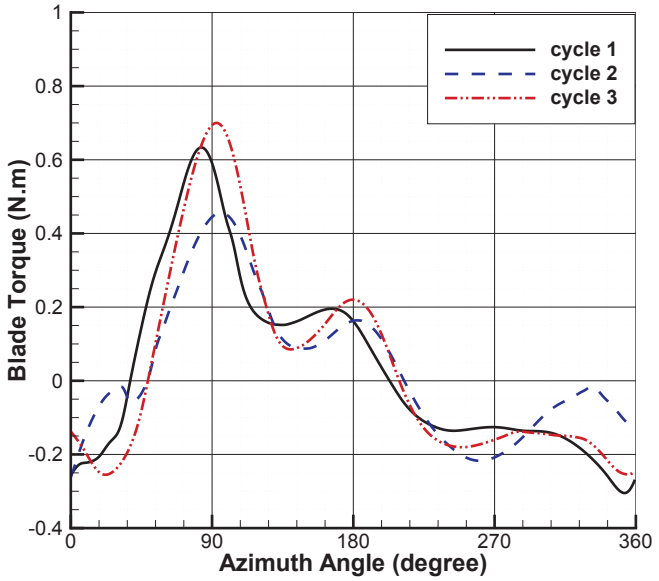

Figure 46: T_b versus azimuth angle for the downwind rotor

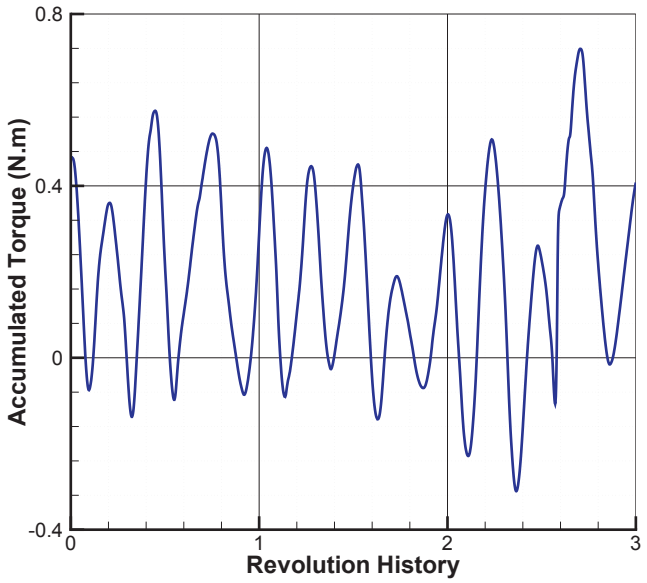

Figure 47: T_t versus revolution history for the downwind rotor

Figures 48 and 49 illustrate the contours of velocity magnitude and turbulence intensity in the wake, respectively. Compared to the wake of the upstream rotor, the downwind turbine exhibits higher flow disturbances in the wake.

Table 4 presents the values of C_p for the downstream VAWT. With 6 m or $15D$ spacing, the time-averaged C_p of the downwind rotor is equal to 1/3 of that of the upwind rotor that is 0.12. This indicates that the M23 model is not an appropriate rotor to be used in the VAWT farms.

Table 4: Values of C_p for the downwind VAWT at $\lambda = 1$

	cycle 1	cycle 2	cycle 3	average of 3 cycles
C_p	0.05	0.03	0.04	0.04

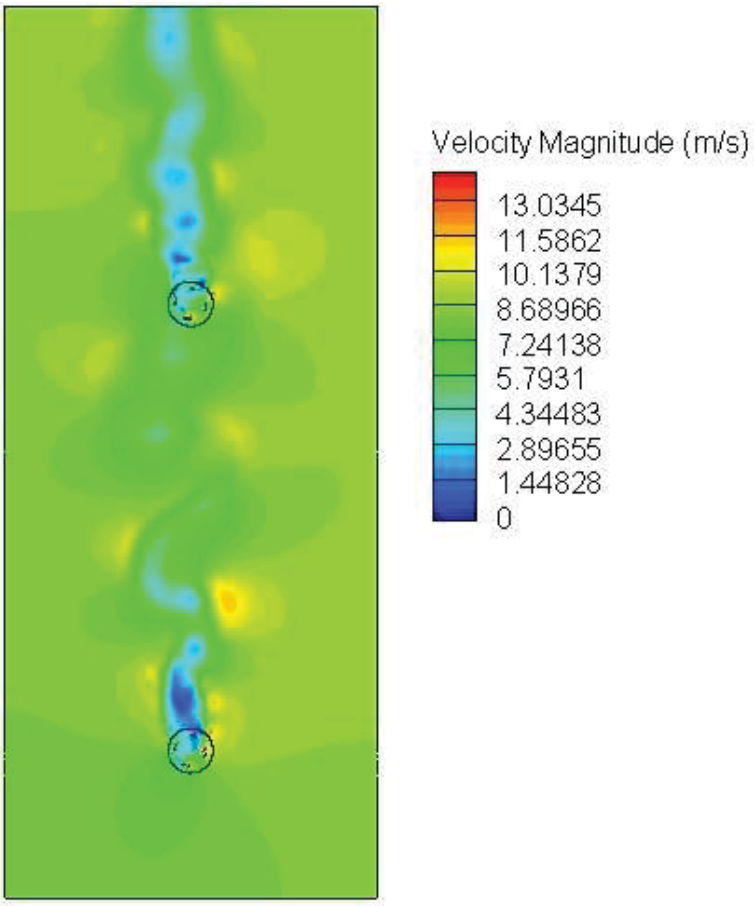

Figure 48: Contours of velocity magnitute (m/s)

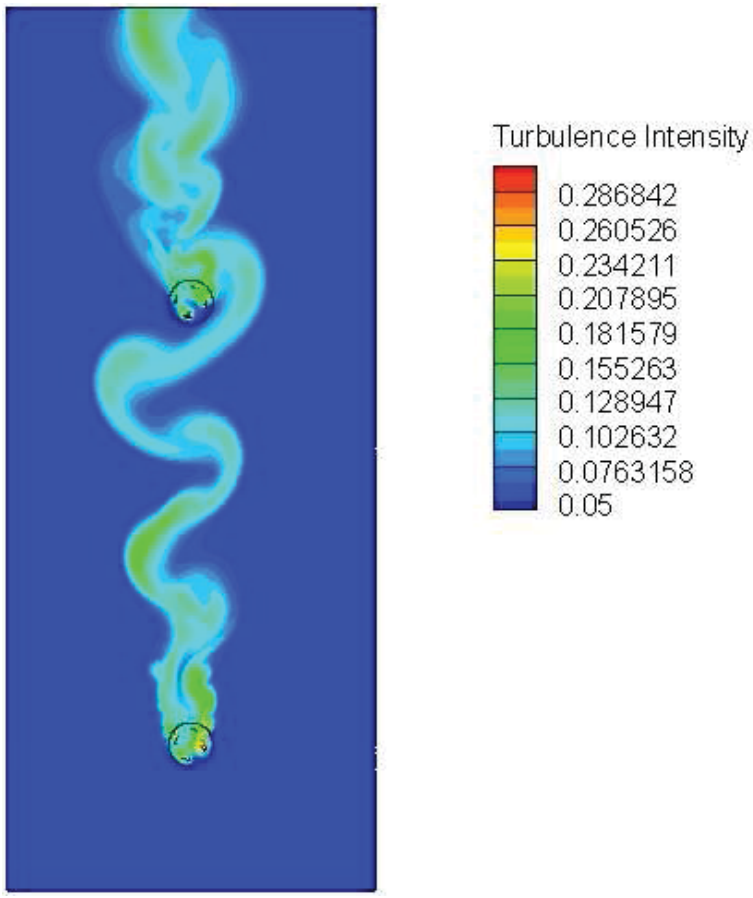

Figure 49: Contours of turbulence intensity

6 Conclusion

A computational study of the aerodynamics of vertical-axis wind turbines (VAWTs) was conducted using the renormalization group (RNG) $k-\varepsilon$ and Spalart-Allmaras (S-A) turbulence models. The rotors were straight-bladed wind turbines analysed with 2-D and 3-D geometries that were generated and meshed in Gambit®. The commercial computational fluid dynamics (CFD) code ANSYS® FLUENT® release 12.1.4 was used for the simulation. The results were compared with numerical and experimental data available in the literature for verification and validation purposes. Two major areas of interest i.e. the torque generated by the VAWTs and the flow disturbances in the wake were specifically investigated. In this regard, velocity, turbulence intensity, and vorticity in the wake play a major role.

The torque output can be analysed when its cycle-averaged values do not change in time and its variation becomes oscillatory and periodic. Nevertheless, the aerodynamics of the wake are not considered to be quasi-steady before the inlet flow reaches the outlet of the computational domain. The flow time required for the wake to reach a quasi-steady state depends on λ or more specifically on U_∞ and ω.

The major contributions of this study can be summarized as:

• In order to obtain spatial convergence in the solution, fine mesh density is necessary. The mesh size is directly proportional to the value of λ.

• Compared to the first-order solver, the second-order solver gives higher values of T_b.

• The turbulence in the wake predicted by the first-order solver is very diffusive. Thus, the second-order accuracy is necessary for the simulation of the wake-dynamics.

• The values of C_Q and C_P obtained by the 2-D model are higher than those given by the 3-D model.

• In analysis of the torque by 2-D geometries, first-order solver can be more appropriate than the second-order solver. This is because of the fact that the 2-D analyses overestimate the torque.

• Compared to the S-A turbulence model, the RNG $k-\varepsilon$ model reports higher values of C_p.

• Comparison between the torque obtained by the ducted and non-ducted geometries reveals that the cycle-averaged value of torque can be higher in ducted VAWTs.

• The major flow disturbances in the wake appear in $0 < L < R$.

• The highest values of $\vec{\omega}$ in the wake are reported mainly positive for $0 < L < R$. Nevertheless, for $-R < L < 0$, maximum values of $\vec{\omega}$ are mainly negative.

7 Future Work

Numerical and experimental study of the VAWTs is a relatively new subject that has created novel motivations for the aerodynamics enthusiasts. The future work in this area, including, but not limited to the following subjects can result in a deeper understanding of the highly complex aerodynamics of the VAWTs:

• In this study, each 2-D simulation with fine mesh density and the 3-D simulation were run using parallel computing on 32 or 64 nodes for 3 to 6 weeks. This computational cost is not always affordable. Therefore, development of a specialized code based on the optimized finite elements and faster solvers can be a huge leap in CFD analysis of the VAWTs.

• Improvement of the accuracy of the RANS solvers in order to capture the dynamic stall.

• Downstream spacing constraints of the VAWTs in wind farms.

• Analysis of performance of downstream VAWTs with different rotor dimensions in wind farms.

• Analysis of possibility of introducing a correction factor for numerical estimation of the torque output from the VAWTs from 2-D geometries.

• Effect of the counter-rotating configuration of VAWTs on the generated torque.

• Study of the effect of the HAWTs' wake on the performance of the VAWTs and vice versa.

References

[1] X. Ji and J. Schluter. Design and analysis of small-scale vertical axis wind turbine. In *Renewable Power Generation (RPG 2011), IET Conference on*, pages 1–10. IET, 2011.

[2] Louis Angelo Danao. The influence of unsteady wind on the performance and aerodynamics of vertical axis wind turbines. 2012.

[3] J.O. Dabiri. Potential order-of-magnitude enhancement of wind farm power density via counter-rotating vertical-axis wind turbine arrays. *Journal of Renewable and Sustainable Energy*, 3:043104, 2011.

[4] Akiyoshi Iida, Akisato Mizuno, and Keiko Fukudome. Numerical simulation of aerodynamic noise radiated form vertical axis wind turbines. In *Proceedings of the 18 International Congress on Acoustics*, 2004.

[5] R.W. Whittlesey, S. Liska, and J.O. Dabiri. Fish schooling as a basis for vertical axis wind turbine farm design. *Bioinspiration & Biomimetics*, 5:035005, 2010.

[6] D. Tromeur-Dervout, G. Brenner, D.R. Emerson, and J Erhel, editors. *Parallel Computational Fluid Dynamics 2008*, volume 74 of *Lecture Notes in Computational Science and Engineering*. Springer, 2010.

[7] J.F. Manwell, J.G. McGowan, and A.L. Rogers. *Wind energy explained*. Wiley Online Library, 2002.

[8] C.S. Ferreira, G. van Bussel, and G. van Kuik. 2d cfd simulation of dynamic stall on a vertical axis wind turbine: verification and validation with piv measurements. In *45th AIAA Aerospace Sciences Meeting and Exhibit/ASME Wind Energy Symposium*, 2007.

[9] I. Paraschivoiu. *Wind turbine design: with emphasis on Darrieus concept*. Montreal: Polytechnique International Press, 2002.

[10] R. Howell, N. Qin, J. Edwards, and N. Durrani. Wind tunnel and numerical study of a small vertical axis wind turbine. *Renewable Energy*, 35(2):412–422, 2010.

[11] S. Mertens, G. Van Kuik, and G. Van Bussel. Performance of an h-darrieus in the skewed flow on a roof. *Journal of Solar Energy Engineering*, 125:433, 2003.

[12] C.J.S. Ferreira, G.J.W. van Bussel, and G.A.M. van Kuik. Wind tunnel hotwire measurements, flow visualization and thrust measurement of a vawt in skew. *Journal of Solar Energy Engineering*, 128:487, 2006.

[13] P.R. Spalart and S.R. Allmaras. A one-equation turbulence model for aerodynamic flows. *La recherche aérospatiale*, 1(1):5–21, 1994.

[14] V. Yakhot and S.A. Orszag. Renormalization group analysis of turbulence. i. basic theory. *Journal of scientific computing*, 1(1):3–51, 1986.

[15] S.A. Orszag, V. Yakhot, W.S. Flannery, F. Boysan, D. Choudhury, J. Maruzewski, and B. Patel. Renormalization group modeling and turbulence simulations. *Near-wall turbulent flows*, pages 1031–1046, 1993.

[16] B.E. Launder and D.B. Spalding. *Lectures in mathematical models of turbulence*. Academic Press, 1979.

[17] ANSYS. *ANSYS FLUENT Theory Guid*. ANSYS, 2010.

[18] N.N. Sørensen and JA Michelsen. Drag prediction for blades at high angle of attack using cfd. *Journal of solar energy engineering*, 126:1011, 2004.

[19] Chao Li, Songye Zhu, You-lin Xu, and Yiqing Xiao. 2.5 d large eddy simulation of vertical axis wind turbine in consideration of high angle of attack flow. *Renewable Energy*, 51:317–330, 2013.